Microscopy analysis of soils at the Phoenix landing site, Mars: Classification of soil particles and description of their optical and magnetic properties

W. Goetz,[1] W. T. Pike,[2] S. F. Hviid,[1] M. B. Madsen,[3] R. V. Morris,[4] M. H. Hecht,[5] U. Staufer,[6] K. Leer,[3] H. Sykulska,[2] E. Hemmig,[2] J. Marshall,[7] J. M. Morookian,[5] D. Parrat,[8] S. Vijendran,[2] B. J. Bos,[9] M. R. El Maarry,[1] H. U. Keller,[1] R. Kramm,[1] W. J. Markiewicz,[1] L. Drube,[3] D. Blaney,[5] R. E. Arvidson,[10] J. F. Bell III,[11] R. Reynolds,[12] P. H. Smith,[12] P. Woida,[12] R. Woida,[12] and R. Tanner[12]

Received 26 May 2009; revised 4 December 2009; accepted 11 January 2010; published 4 August 2010.

[1] The optical microscope onboard the Phoenix spacecraft has returned color images (4 μm pixel^{-1}) of soils that were delivered to and held on various substrates. A preliminary taxonomy of Phoenix soil particles, based on color, size, and shape, identifies the following particle types [generic names in brackets]: (1) reddish fines, mostly unresolved, that are spectrally similar to (though slightly darker than) global airborne dust [*red fines*], (2) silt- to sand-sized brownish grains [*brown sand*], (3) silt- to sand-sized black grains [*black sand*], and (4) small amounts of whitish fines, possibly salts [*white fines*]. Most particles have a saturation magnetization in the range 0.5-2 Am^2 kg^{-1} as inferred from their interaction with magnetic substrates. The particle size distribution has two distinct peaks below 10 μm (fines) and in the range 20–100 μm (grains), respectively, and is different from that of ripple soils in Gusev crater. In particular medium to large sand grains appear to be absent in Phoenix soils. Most sand grains have subrounded shape with variable texture. A fractured grain (observed on sol 112) reveals evidence of micrometer-sized crystal facets. The brown sand category displays a large diversity in color including shiny, almost colorless particles. Potential source regions for these grains may be the Tharsis volcanoes or Heimdal crater (20 km east of the landing site). The black grains are suggested to belong to a more widespread population of particles with mafic mineralogy. The absence of black/brown composite grains is consistent with different formation pathways and source regions for each grain type.

Citation: Goetz, W., et al. (2010), Microscopy analysis of soils at the Phoenix landing site, Mars: Classification of soil particles and description of their optical and magnetic properties, *J. Geophys. Res.*, *115*, E00E22, doi:10.1029/2009JE003437.

1. Introduction

[2] The Phoenix (PHX) spacecraft landed on 25 May 2008 in the northern Martian plains at 68.2°N, 234.3°E (aerocentric coordinates). The geologic context is described in detail elsewhere [*Smith et al.*, 2009; *Arvidson et al.*, 2009; *Heet et al.*, 2009]. Briefly, the landing site is situated about 1500 km north of the northern border of the Tharsis plateau and about 1800 km north of the center of Alba Patera, a major volcanic construct in the northernmost part of Tharsis. It is located ~500 km from the nearest lava flows from Alba Patera and about the same distance from the nearest dark circumpolar dunes [*Herkenhoff and Vasavada*, 1999; *Tanaka and Hayward*, 2008, *Tanaka et al.*, 2008]. The landing site is ~20 km west of Heimdal crater (11.5 km in diameter). The lander touched down on the so-called Scandia formation that

[1]Max Planck Institute for Solar System Research, Katlenburg-Lindau, Germany.
[2]Department of Electrical and Electronic Engineering, Imperial College, London, UK.
[3]Niels Bohr Institute, University of Copenhagen, Copenhagen, Denmark.
[4]NASA Johnson Space Center, Houston, Texas, USA.
[5]Jet Propulsion Laboratory, California Institute of Technology, Pasadena, California, USA.
[6]Micro and Nano Engineering Laboratory, Delft University of Technology, Delft, Netherlands.
[7]SETI Institute, Mountain View, California, USA.
[8]Institute of Microtechnology, University of Neuchâtel, Neuchâtel, Switzerland.
[9]NASA Goddard Space Flight Center, Greenbelt, Maryland, USA.
[10]Department of Earth and Planetary Sciences, Washington University in St. Louis, St. Louis, Missouri, USA.
[11]Department of Astronomy, Cornell University, Ithaca, New York, USA.
[12]Lunar and Planetary Laboratory, University of Arizona, Tucson, Arizona, USA.

Copyright 2010 by the American Geophysical Union.
0148-0227/10/2009JE003437

surrounds the northern border of the Tharsis plateau and is interpreted as volcanic ash and/or polar deposits. The lander is sitting on partially eroded ejecta deposits from Heimdal crater. Material observed in the microscopic images may thus have contributions from both volcanic and impact processes.

[3] The goal of the present paper is a classification and description of different particle types seen in the microscopic images. Whenever possible, the observations are discussed in relation to similar data from other missions, in particular data from the Mars Exploration Rover Mission to Gusev crater.

2. Instruments and Operations

[4] Phoenix operations are described in detail by *Arvidson et al.* [2009]. In general, soil material was scooped up and imaged by the Surface Stereo Imager (SSI) and Robotic Arm Camera (RAC) [*Keller et al.*, 2008]. The RAC images were most often taken in color mode, i.e., as three successive images with red, green, and blue light emitting diodes (LEDs) switched on, and a fourth one with all LEDs switched off. When imaging the scoop divot (depression cut out near the front of the blade of the scoop at the end of the Robotic Arm (RA) [see *Arvidson et al.*, 2009, Figure 2], high resolution mode (22 μm pixel^{-1}) was used. After image documentation, soil samples were transferred to various substrates (microbucket, micromachined silicon grid, weakly, or strongly magnetic and sticky silicone) [*Hecht et al.*, 2008; *Leer et al.*, 2008] for further imaging by the Optical Microscope (OM). The OM images (4 μm pixel^{-1}) include color information, as they were taken as three successive images with two red, two green, and two blue LEDs switched on. A fourth image with all LEDs switched off was not needed, as the OM is in a light-tight box [*Hecht et al.*, 2008]. Unlike the RAC, the OM is a fixed focus camera, and the sample is brought into focus position by the Sample Wheel Translational Stage (SWTS). The in-focus imaged area is 2 mm × 1 mm. Most of the results on the optical properties of Phoenix soil particles reported in the present paper were obtained from OM images.

[5] The study of particle sizes is based on both OM and RAC images to facilitate comparisons to size distributions obtained for Gusev soils. Size analysis of Phoenix soil and dust particles down to the submicron scale was done by inclusion of Atomic Force Microscope (AFM) data [*Pike et al.*, 2009; W. T. Pike et al., The particle size distribution of the Martian soil at the Phoenix landing site, manuscript in preparation, 2010]. Images used in the present paper are specified by the mission identifier, an (optional) instrument identifier, the sol number, and the last four digits of the spacecraft clock time. The following instruments (besides the ones onboard Phoenix) have provided data that are used in the present paper: The Microscopic Imager (MI) and the Navigation Camera (Navcam) onboard the Mars Exploration Rovers (MER-A, MER-B), the Compact Reconnaissance Imaging Spectrometer for Mars (CRISM) onboard the Mars Reconnaissance Orbiter (MRO), and the Wide Field Planetary Camera-2 (WFPC-2) onboard the Hubble Space Telescope (HST).

[6] The spacecraft clock time appears both in the file name and in the header of the data as archived in the Planetary Data System (PDS; cf. http://pds.jpl.nasa.gov/) and designates the image acquisition time expressed in number of seconds that elapsed since 6 January 2000, 0000:00 UTC. Virtually any image (or RGB image triplet) is uniquely specified by the combination of mission name, sol number, and the last four digits of the spacecraft clock time. For RGB color composites of PHX-OM images these four digits will refer to the red image.

[7] The calibration pipeline for OM images applies to the 12 bit raw images [*Hecht et al.*, 2008] and involves the following steps: (1) bad and hot pixel removal, (2) bias subtraction, (3) dark current subtraction, (4) conversion to units [DN/s], (5) flat fielding, and (6) conversion to reflectance R*. Steps 1–5 are standard calibration steps [see, e.g., *Bell et al.*, 2006]. Step 5 involves division of the image by a flat field correction array that has a mean value equal to unity. The images that are referred to as RAD calibrated images (in units [DN/s]) have been processed as described in steps 1–5. Step 6 involves the division of the output image from step 5 by a similarly illuminated and calibrated image of the sol 4 white target [*Hecht et al.*, 2008], and a correction for changes in radiant output of the LEDs over the course of the mission. Prior to this division the white target images are flattened by the means of a multiple-order polynomial fit function. This procedure removes granularity and surface roughness, which are inherent properties of the white target.

[8] Changes of the LEDs' radiant output as a function of mission time were inferred from the radiant power reflected by typical dusty regions in the RAD calibrated images. First such regions were selected manually in a large number of images that were acquired throughout the mission. Then the average values of these regions were plotted as a function of sol number and fitted by a straight line.

[9] Obviously this procedure is based on the assumption that typical dust can be easily recognized in all images and has stable optical properties as a function of time and dig location. The procedure was cross checked against repeated images of the white target (sols 4, 57, 111, 117, 120, 121, and 137) that became increasingly contaminated by dust. It was inferred that the output of the blue, green and red LEDs changed by (+4.1 ± 1.0)%, (+2.0 ± 1.0)%, and (−8.7 ± 2.0)%, respectively, over the course of 100 sols. Thus the output of the blue and green LEDs increased very slightly over the course of the mission, while that of the red LEDs decreased by about 10%, which is qualitatively in agreement with premission expectations for the LED types used [*Reynolds et al.*, 2008]. The above numbers were used in calibration step 6.

[10] Strictly speaking we do not know if the signal changes (as inferred from the RAD images) were caused by changes of the LED output and/or by changes of the CCD sensitivity. These changes could in turn be caused by the number of operational CCD/LED hours or by the temperature of any of these devices. We were unable to distinguish between these different potential causes. Fortunately the above corrections remain valid, whatever may be the causes of these signal changes.

[11] The lighting and viewing geometry for the OM is largely bidirectional. Each point on a given substrate is generally illuminated by two LEDs of a given color (belonging to clusters 1 and 2; see Figure 1). Given the divergence of the incident light beams (~10°) the local incidence angles at each point of the substrate are clustered within a few degrees around average values of 29.8° (red and blue

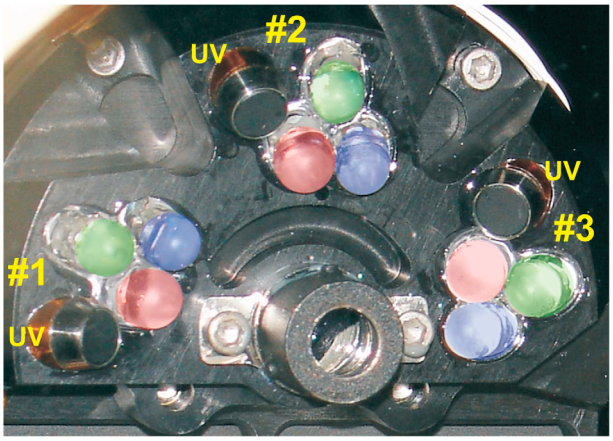

Figure 1. Lighting geometry for OM images. Each LED cluster (labeled as 1, 2, or 3) contains three VIS LEDs and one UV LED. The VIS LEDs have been colorized in order to specify the relative position of each LED type. The LEDs are located on two concentric circles around the optical axis with radii of 14.4 mm and 19.1 mm and make an angle of 29.8° and 37.2° with the optical axis, respectively. The distance from the end of the LED to the target is about 25 mm (red and blue LEDs) and 28 mm (green LEDs). Refer also to *Hecht et al.* [2008]. During the mission the large majority of all images were acquired by using LED clusters 1 and 2. LED cluster 3 was rarely used due to undesired scattering effects on the AFM cantilevers.

LEDs) and 37.2° (green LEDs). The illumination becomes slightly conical, as the front windows of the LEDs were diffused preflight using a fine grinding compound in order to achieve even illumination of the substrates. The reflected light is captured and detected within an approximately 20° wide cone that is centered around the surface normal to the substrate so that emission angles are clustered around an average value of 0° [*Hecht et al.*, 2008]. As mentioned above the incident light arrives from two different directions. However, each illuminating LED should contribute equally to the total reflectance, assuming equal radiant output from both LEDs and assuming random orientation of the light scattering particles on the substrate. Therefore, the lighting-viewing geometry may be termed bidirectional rather than tridirectional. Since the images are ratioed to white target images that have been acquired at the very same geometry, the inferred reflectance is R* to the extent that the white target matches a perfectly diffuse (Lambertian) surface [*Reid et al.*, 1999; *Bell et al.*, 2008].

3. Analysis

[12] This section describes optical properties (section 3.1), morphology and surface textures (section 3.2), magnetic properties (section 3.3), and size analysis (section 3.4) of Phoenix soil particles. The optical properties will provide the basis for a classification scheme of the larger (silt to sand sized) grains. In section 3.5 the data presented on Phoenix soil particles will be put into context by comparison to other data sets.

3.1. Optical Properties of Soil Particles

[13] A total of eight soil samples were delivered to the OM during the mission. Detailed descriptions of sampling locations are provided by *Arvidson et al.* [2009]. The samples will be discussed in order of delivery to the OM. In some cases, images acquired long after the delivery sol have better quality and were therefore used in the present study (Table 1), although they might be affected by cross contamination among different substrate sets.

3.1.1. Spectral Reflectance

[14] This section describes the optical properties of the eight strong magnet samples specified above. Figure 2a shows images of the soil samples selected for further analysis. All samples were accumulated on the strongly magnetic substrate (hereafter referred to as the "strong magnet"). In each image (Figure 2b) a region of interest (ROI) containing a thick, in-focus layer of soil is manually defined. This ROI is termed "all." Poorly covered or out-of-focus regions are discarded from that ROI. The soil samples that were accumulated on the strong magnets show in general the largest grain diversity, so they were used for detailed analysis.

[15] Phoenix soil particles are bimodal both in terms of size and albedo. This very simple statement can be confirmed by visual inspection of Figure 2a. The smallest particles, often unresolved, are predominantly red, while larger grains (typically in the size range 20–100 μm) are dark (mostly brownish or black), and in some cases almost transparent. Most of the larger grains have a significantly flatter (less red) reflectance spectrum than the unresolved fines. According to *Wentworth* [1922] clay-sized and silt-sized particles have maximum diameters of 3.9 μm (1/256 mm) and 62.5 μm (1/16 mm), respectively. Grains larger than 62.5 μm are termed sand-sized particles. Thus the grains encountered in Phoenix soils

Table 1. Overview of Phoenix Soil Samples[a]

Set	Sample	Delivery Sol	Images Studied	Source Trench and Sample Type
2	Mama Bear	17	R, sol 31, 5549; G, sol 31, 5578; B, sol 31, 5608	Dodo Goldilocks trench, surface sample
1	Rosy Red	26	R, sol 33, 4125; G, sol 33, 4155; B, sol 33, 4184	Rosy Red trench, surface sample
10	Sorceress	38	R, sol 44, 1565; G, sol 44, 1595; B, sol 44, 1625	Snow White trench, scraped pile above ice
8	Mother Goose	67	R, sol 122, 7924; G, sol 122, 7954; B, sol 122, 7984	trench and type of sample unknown
7	Wicked Witch	75	R, sol 122, 0014; G, sol 122, 0044; B, sol 122, 0073	Snow White trench, scraped pile above ice
6	Golden Key	99	R, sol 103, 6251; G, sol 103, 6281; B, sol 103, 6311	Dodo Goldilocks trench, lag deposit scraped pile above ice
5	Golden Goose	110	R, sol 112, 1338; G, sol 112, 1368; B, sol 112, 1399	Stone Soup trench, subsurface sample
4	Galloping Hessian	128	R, sol 132, 9135; G, sol 132, 9165; B, sol 132, 9195	surface sample below the rock Headless that was flipped over into the Neverland trench on sol 117

[a]The images listed in the fourth column (specified by the last four digits of the spacecraft clock time, see section 2) are the complete data basis for Figures 2–5.

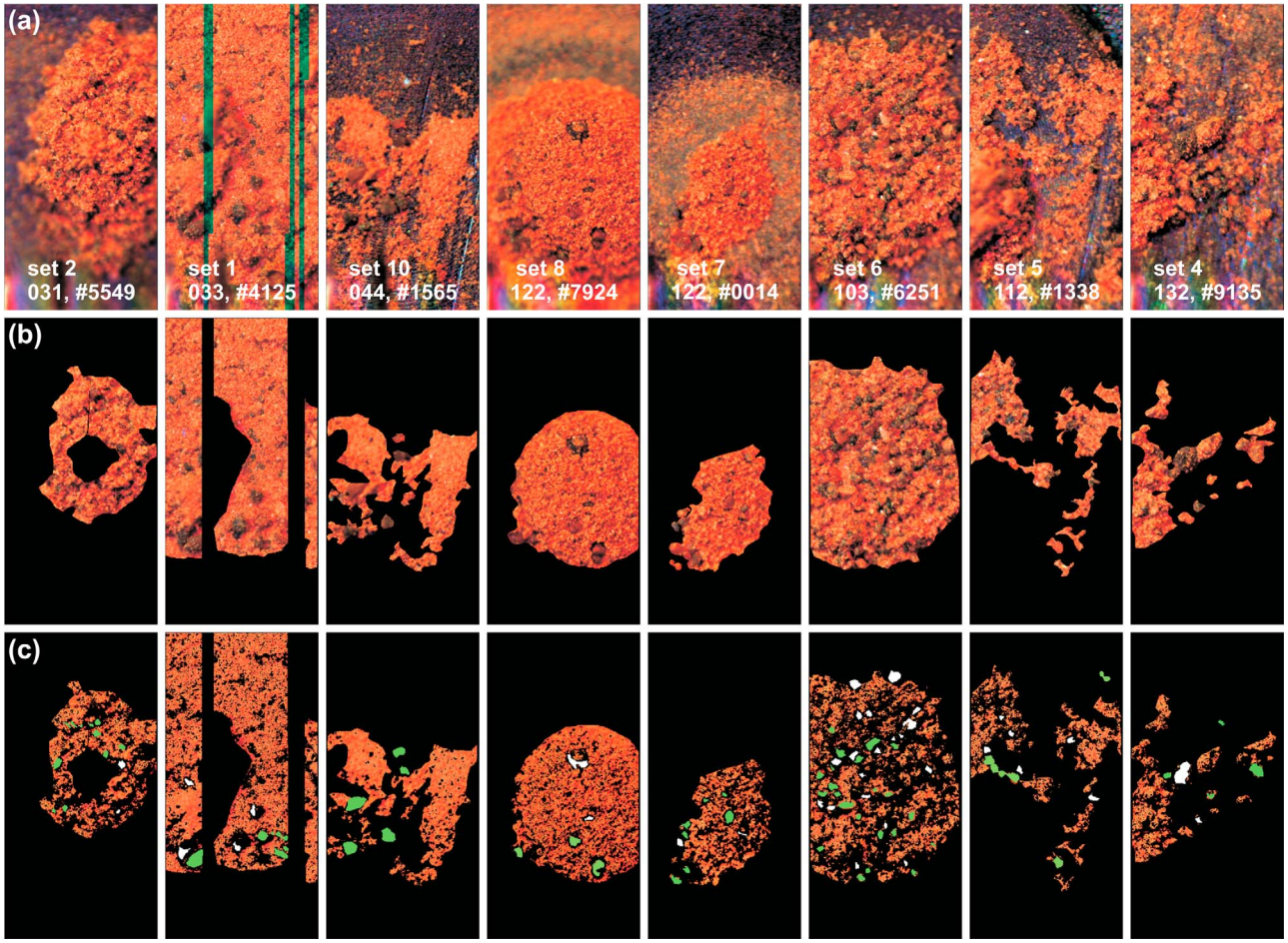

Figure 2. (a) Approximate true color images of Phoenix soil samples on the strongly magnetic substrate. The images are specified by the sol number, the identifier of the red image (four last digits of the spacecraft clock time), and the substrate set. (b) Region of interest (termed "all") that is used for the study of the optical properties. The discarded regions (uncovered substrate, out-of-focus regions) are blacked out. (c) Further regions of interest that are essentially subregions of Figure 2b. The dusty regions (ROI termed "red fines") are shown as they appear in the color images. The nonobstructed parts of black and brown grains are represented as uniform white and green regions, respectively. Thus, the individual blotches do not match the outline of the corresponding particle. The precise definition of these ROIs is given in the text.

are partly silt and partly sand sized. However, for the sake of simplicity we will refer to all of these grains as "sand grains," although an appreciable fraction of them are silt sized.

[16] Figure 2c shows different ROIs that refer to different particle types in these soils. These ROIs are largely contained by the above defined ROI "all" and were selected in different ways: The reddish fines (bright red soil or airborne dust) were selected by requiring a reflectance $R^* < 0.1$ in the blue and $R^* > 0.2$ in the red channel, respectively. Among the larger grains two populations could be distinguished by visual inspection in all soil images and these were hand selected: brownish particles with a wide spectral range and black particles.

[17] Figure 3 plots the optical characteristics (in terms of R* reflectance) of each ROI or type of particles as defined in Figure 2. The reflectance of the ROI "all" (Figure 3a) and that of the fine reddish material (Figure 3b) does not show an overall (upward or downward) trend, as this is inhibited by the RAD calibration procedure (section 2). In fact this procedure corrects for a linear overall change in LED radiant power (or camera sensitivity), but does not erase potential fine differences between different soil samples (or substrate sets).

[18] For each particle type (Figures 3b–3d), both the simple pixel averages (crosses) and the Gaussian fit parameters (open circles) are presented. The center reflectance as inferred from the Gaussian fit is often lower than the corresponding ROI average. This is particularly the case for the red reflectance of the fine reddish material (Figure 3b), which in turn is related to the way this material was defined: The requirement was a blue and red reflectance below 0.1 and above 0.2, respectively. This condition is somewhat arbitrary, but allows the selection of pixels dominated by a type of material that is a well-known and well-characterized alteration end-member on the surface of Mars. For many Phoenix soils, most pixels selected in that way do indeed have a red reflectance around 0.2, and fewer pixels have larger reflectance (up to 0.3 or even 0.4). In this case the ROI average reflectance will be some-

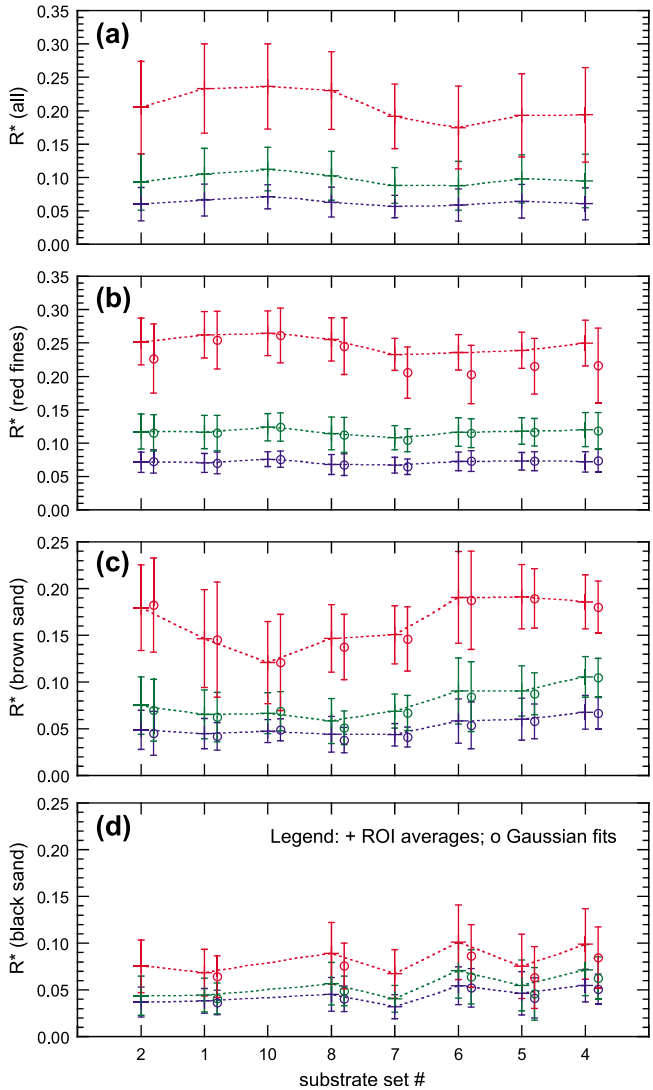

Figure 3. Optical characteristics of Phoenix soil particles. (a) ROI "all." (b) ROI "red." (c) ROI "brown." (d) ROI "black" (see Figure 2). Each graph displays the R* reflectance (red on top, blue on bottom, green between these two) sorted according to substrate set number. In each graph both the ROI averages (crosses) and the Gaussian fits (open circles) are shown. In some cases a meaningful Gaussian fit was not possible due to a low number of data points. The ROI averages are connected by a dotted line in order to guide the eye. Brown sand particles are spectrally diverse and therefore have a strongly varying reflectance with large relative uncertainty. The set number specifies the images that were used for these plots (Table 1).

what larger than 0.2, while the Gaussian fit takes the shape of the reflectance histogram into account and provides a center reflectance of about 0.2. Pixels with a reflectance below 0.2 have not been selected, because they do not meet the above conditions and would have likely contained some mixed pixels, such as pixels of brownish sand particles that are partially contaminated by reddish material. The Gaussian fits were excellent in most cases and therefore the use of Gaussian fit parameters is favored over simple ROI averages.

[19] The spectral properties of the brownish grains (Figure 3c) appear to vary between different Phoenix soil samples, and additionally have a large relative uncertainty computed as the standard deviation of the associated ROI. Both facts attest to the large diversity of this type of grains as compared to the black ones (Figure 3d). In the remainder of this paper only a minimum number of categories shall be defined for Phoenix soil particles, and no objective criteria could be found for further subdivision of the brown sand grains.

[20] Figure 4 shows scatter plots of the reflectance and the spectral slope for all soil samples presented in Figure 2. Pixels in the ROI "all" are shown as small black dots. Pixels covered by the other ROIs shown in Figure 2 have been plotted as black crosses, blue crosses and red dots for the black grains, brownish grains and reddish fines, respectively. Note that pixels belonging to the ROI "all" (Figure 2b), but not to any of the remaining ROIs (Figure 2c), are actually "bad pixels" in the sense of badly illuminated soil patches on the substrate. The number of such bad pixels generally increases with the height and relief of soil material on the substrate. The plots shown in Figures 4g and 4h have a comparatively large amount of such bad pixels. In one case (Figure 4f, or set 6) the region representing the brownish particles overlaps strongly with the one representing the reddish fines. This feature indicates strong contamination of sand particles by reddish fines. It is remarkable that precisely that sample was a sublimation lag (see Table 1), where finely divided and strongly coloring reddish material was amply available after the freeze dry process.

[21] In summary we have identified and characterized three different types of soil particles: Reddish (unresolved) fines, dark (almost black) grains, and brownish grains. Hereafter, we will adopt the nomenclature "red fines," "black sand" and "brown sand," respectively. These are simple generic terms that are based on a qualitative color analysis. Virtually all particles in the Phoenix (and more generally Martian) soils are characterized by a ferric absorption edge that imparts a reddish color. Obviously the average of all these spectra would be reddish as well. The above naming convention characterizes in a qualitative way the deviation from that average spectrum. The ROIs corresponding to each particle type are named accordingly: "red," "black" and "brown" designate the ROIs that are associated with red fines, black sand, and brown sand, respectively.

3.1.2. Whitish Particles

[22] In addition to red fines and black and brown sand-sized particles, we can distinguish by visual inspection of the images a fourth particle type: flakes of varying extension composed of unresolved whitish particles. A systematic study of brightness histograms also provides evidence for the presence of such particles. The major question to be addressed is the following: How can "whitish particles" be defined in a rigorous way?

[23] The approach we used is based on plotting the number of pixels that exceed a given reflectance (R*) versus that reflectance. More specifically, this plot (from hereon referred to as threshold plot, TP) is drawn for pixels in the red image. The algorithm involves the following two steps: (1) A first

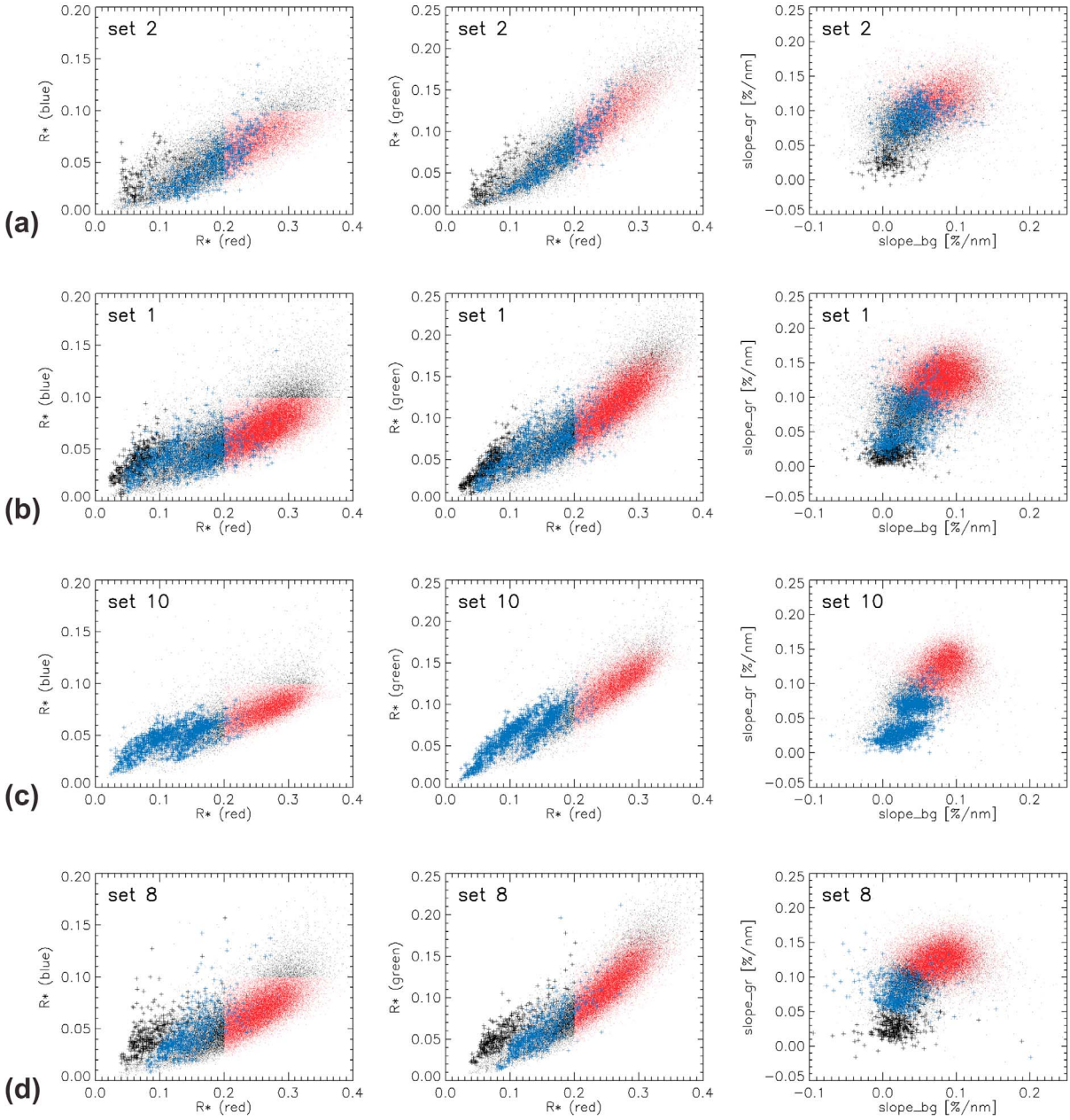

Figure 4. (a–d) Scatterplots of the optical properties of Phoenix soil samples. Each row corresponds to the strong magnet of a given set of OM substrates with the following plot types (from left to right): Blue reflectance versus red reflectance, green reflectance versus red reflectance, and green-red slope of the reflectance versus blue-green slope. The axis limits are the same for each plot type in order to facilitate comparison between different soil samples. In each graph "all" pixels (Figure 2b) are shown as black dots, whereas pixels covered by the ROIs shown in Figure 2c have been plotted as black crosses, blue crosses, and red dots for the black grains, brownish grains, and reddish fines, respectively. The set number specifies the images that were used for these plots (Table 1). (e–h) Scatterplots of the optical properties of Phoenix soil samples (continued). Each row corresponds to the strong magnet of a given set of OM substrates.

plot, TP1, is drawn for all pixels within the ROI "all." (2) A second one, TP2, is drawn for a subset of pixels within the ROI "all." All pixels within that subset are required to meet the same conditions as red fines (see section 3.1.1): R*(blue) < 0.1 and R*(red) > 0.2. Both plots, TP1 and TP2, are normalized to 100%. Then TP1 characterizes the actual brightness of all pixels in the given ROI (ROI "all"), while TP2 represents the curve one would expect, if only classical reddish soil or dust was present. The intersection between these two curves is referred to as "threshold reflectance" (or R_t*).

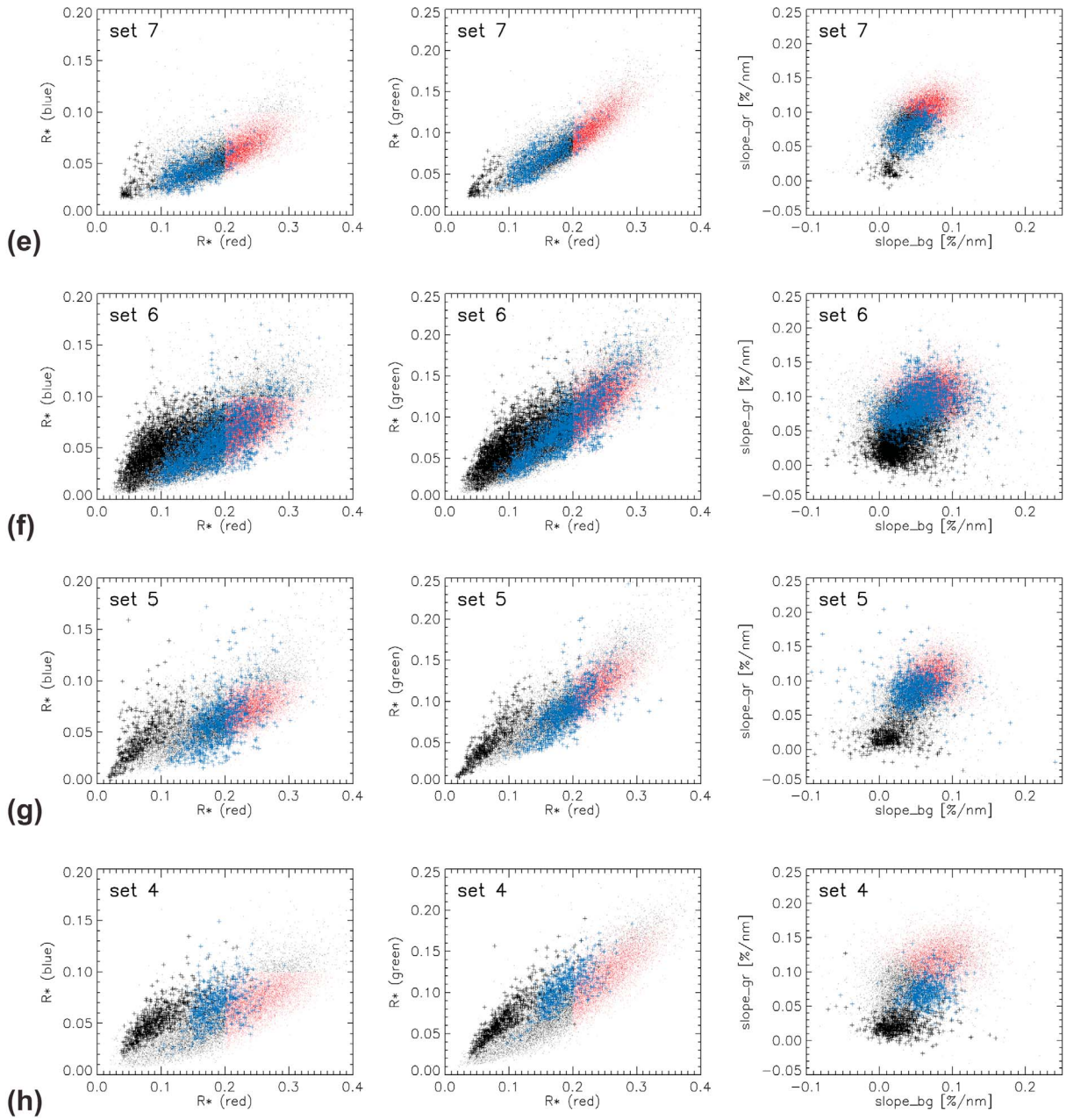

Figure 4. (continued)

[24] In Figure 5 TP1 (red, solid line) and TP2 (black, dashed line) are drawn for the red reflectance of each soil sample and the intersection (R_t*) is determined. The goal is to quantify the fraction of particles brighter than R_t*. A subset of those particles that are reasonably bright in the entire visible range (with R*(red) > R_t* and R*(green) > 0.2 and R*(blue) > 0.1) are referred to as "whitish particles." Those particles could be salt-rich or icy particles or bright mineral grains such as feldspar. The fraction of respective particles is expressed in pixel % (or areal %).

[25] The unit pixel % is similar to volume % to the extent that the relevant sample on the OM substrate is well mixed. That requires in particular that the sample is not layered or selected according to depth.

[26] Table 2 summarizes the results. The numbers depend on the definition of red (dust like) Martian material and are therefore model-dependent, but they do allow a relative comparison between different Phoenix soil samples. Both Table 2 and Figure 5 show that the inventory of bright particles (i.e., fines that are "more white" than any other soil component) varies between the different soil samples, but is always below 1 pixel % (or volume %) in agreement with results obtained by *Sykulska et al.* [2009].

[27] The uncertainty on the abundances listed in Table 2 is of the order of a factor of two. Despite that large uncertainty

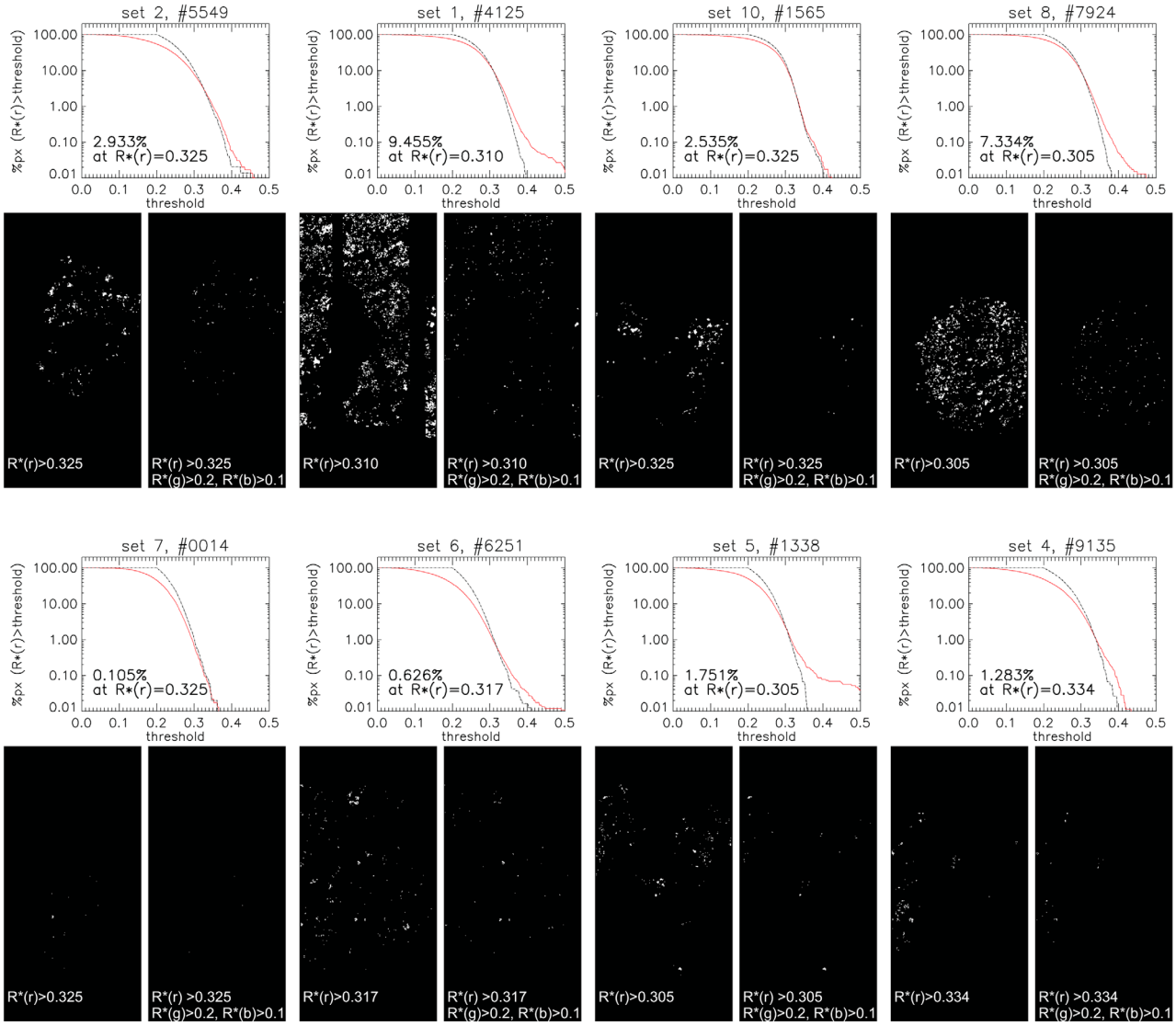

Figure 5. Location of bright (whitish) fines in Phoenix soil samples that were accumulated on the strong magnet. For each of the eight samples the location of high red albedo particles (left) and the whitish subset of these particles (right) is shown. The associated graphs plot the relative fraction (%) of pixels that are brighter than the reflectance read on the abscissa. The red curve refers to the ROI "all" (see Figure 2b). The black curve refers to all pixels inside that ROI which have the typical spectral characteristics of red fines (R*(blue) < 0.1 and R*(red) > 0.2). The intersection between both curves is termed the "red threshold reflectance" (R_t*). White fines are defined to have a reflectance (R*) that is larger than 0.1, 0.2, and R_t* in the blue, green, and red channel, respectively.

Table 2. Presence of Bright Particles in Phoenix Soil Samples[a]

Set	Sample	Red Threshold Reflectance (R_t*)	Fraction [pixel %] of Excessively Red Particles With R*(red) > R_t*	Fraction [pixel %] of Whitish Particles With R*(red) > R_t*, R*(green) > 0.2, R*(blue) > 0.1*
2	Mama Bear	0.325	3	0.4
1	Rosy Red	0.310	9	0.6
10	Sorceress	0.325	3	0.2
8	Mother Goose	0.305	7	0.4
7	Wicked Witch	0.325	0.1	0.01
6	Golden Key	0.317	0.6	0.1
5	Golden Goose	0.305	2	0.3
4	Galloping Hessian	0.334	1	0.3

[a]According to the rightmost column the fraction of whitish particles ranges from (almost) 0 to 1 pixel % for all soil samples. Refer to the main text for further details.

the data seem to indicate that the samples scraped near the ice table (Sorceress (set 10), Wicked Witch (set 7), and Golden Key (set 6)) have a lower abundance in whitish material than surface samples. In particular the soil Wicked Witch (set 7) seems to lack almost completely this particular type of material (only 0.01 pixel%).

[28] The abundances of whitish material as inferred from OM images are much below the ones reported for calcium carbonate [*Boynton et al.*, 2009; D. W. Ming et al., manuscript in preparation, 2010], perchlorates [*Hecht et al.*, 2009] and (likely) some sulfates [*Kounaves et al.*, 2010] in the soils. However, most whitish material may be intimately mixed with other soil components and in particular contaminated to a varying extent by the micron-sized fraction of red fines. Hereafter, the whitish fines described in this section will be referred to by the simple generic term "white fines," although they have an absorption edge that results in a reddish color.

3.2. Morphology and Surface Texture of Soil Particles

[29] The scope of this paper is to provide a descriptive survey of color, size, and shape of particles imaged by the OM and to work out a preliminary geological and geochemical interpretation. Figure 6 illustrates the diversity in size and shape of sand-sized particles. The particles are individually numbered. Black and brown sand particles are marked by a solid and a dotted arrow, respectively.

[30] The black sand particles are most often rounded and approximately equidimensional (particles 7, 11, 18), but other shapes are found as well (particles 25, 31, 33). Their color varies from dark gray (black) to slightly reddish (see Figure 3d) presumably depending on the degree of contamination of their surface by red fines. Alternatively their reddish color may be caused by surface stains. Black sand particles are more uniform than brown ones in terms of color and size, but differ from each other by their surface texture which ranges from smooth and shiny (particles 7, 33) to rough (particle 11). The diversity in surface texture may express the varying degree of surface weathering of these particles and/or different (eolian) transport distances. In addition all black particles may not have the same average mineralogy, especially if they have been transported over a longer distance. Their surface contains frequent, highly localized (typically one pixel wide) patches of intense specular reflection (see particles 9 and corresponding inset). In most cases these reflections are green, but also blue and red reflections are observed (see particles 9). This observation indicates the presence of well defined planes that may be fractured glassy surface areas or crystal facets. Particle 10 appears to be a fractured black sand particle (about 60 μm in diameter). This interpretation is based on two observations: (1) The surface in question appears to be flat as inferred from the absence of a distinct brightness gradient across that surface. In this respect particle 10 is very different from particle 7. (2) The potentially broken surface is composed of differently oriented specularly reflecting facets next to each other. Their average reflectance (R*) is 10, 12 and 16% in the blue, green and red channel, respectively. All colors are present and evenly distributed across the fractured surface of the particle indicating a random distribution of facet orientations. The colors do not represent the mineralogy but are artifacts caused by each LED illuminating the sample from a slightly different direction. The facet will glint whenever the condition for specular reflection is fulfilled. An OM image is generally acquired while two LEDs of a given color illuminate the sample with only one contributing to the brightness of that particular facet due to the highly anisotropic nature of specular reflections.

[31] The ~50 reflecting facets are distributed across (roughly) 170 pixels. Thus each facet on average illuminates 3 to 4 pixels. Given a resolution of 4 μm pixel^{-1} at the target we infer the characteristic area within which specular conditions for one illumination angle are maintained. The facets are likely to be crystallite faces of the fractured surface, as conchoidal fractures of a glassy surface would produce a continuous variation in illumination. The majority of crystallites must be above 4 μm size to produce the monochromatic glints observed.

[32] A darker rim appears to encircle the broken surface of particle 10. That rim might be interpreted as being part of

Figure 6. Black and brown grains on the magnetic (Figures 6a–6j) and sticky silicone (Figures 6k–6l) substrates: (a) sol 33, 4125, set 1, strong magnet, (b) sol 58, 4163, set 8, strong magnet, (c) sol 103, 6622, set 6, strong magnet, (d) sol 112, 9825, set 5, weak magnet, (e) sol 132, 9135, set 4, strong magnet, (f) sol 140, 7910, set 1, strong magnet, (g) sol 112, 1338, set 5, strong magnet, (h) sol 122, 8817, set 8, weak magnet, (i) sol 103, 6530, set 6, strong magnet, (j) sol 148, 1698, set 6, strong magnet, (k) sol 132, 1340, set 4, sticky silicone, and (l) sol 132, 2438, set 4, sticky silicone. Figures 6k–6l were acquired after the delivery of the soil sample Galloping Hessian to the OM. All images (Figures 6a–6l) are at the same scale (Figures 6g and 6k, 1000 μm wide; Figures 6i and 6j, 245 μm wide; all other images, 500 μm wide). The yellow framed insets magnify selected details of the corresponding image. All insets are at the same relative scale and have been stretched in the same way in order to allow for relative comparison of the light-scattering properties of the particle surfaces. In some cases (particles 7 and 10) uninterpolated versions of the insets are also provided in order to demonstrate the effect of pixel interpolation. Black and brown sand particles of interest are specified by a solid and a dotted arrow, respectively. These particles are also labeled by a number. Most black particles are rounded, but have different texture (see particles 7, 11, 33). Particle 10 appears to be a fractured black sand particle. The interior shows differently oriented specularly reflecting planes that may be crystal facets. The color of brown particles varies from transparent to dark brown (opaque) (particles 1–6, 8, 12, 13–17, 19–24, 26–30, 32, 34). Also, their size varies considerably: The oval, shiny particles 17 and 23 have a major axis dimension of less than 30 μm, whereas others (e.g., particles 19–20) are in the range 60–80 μm. The transparent particle 26 (shown in two orientations in Figures 6i and 6j) has a major diameter of 130 μm. The particle can also be seen in the image of substrate set 6 in Figure 2. Brown particles are diverse in shape (particles 19 and 21) and surface texture (particles 1–2, 28–30). The strong overall diversity of brown sand particles is interpreted as indicating a stronger susceptibility for comminution and weathering as compared to the black particles. Refer to the main text for further discussion of these particles.

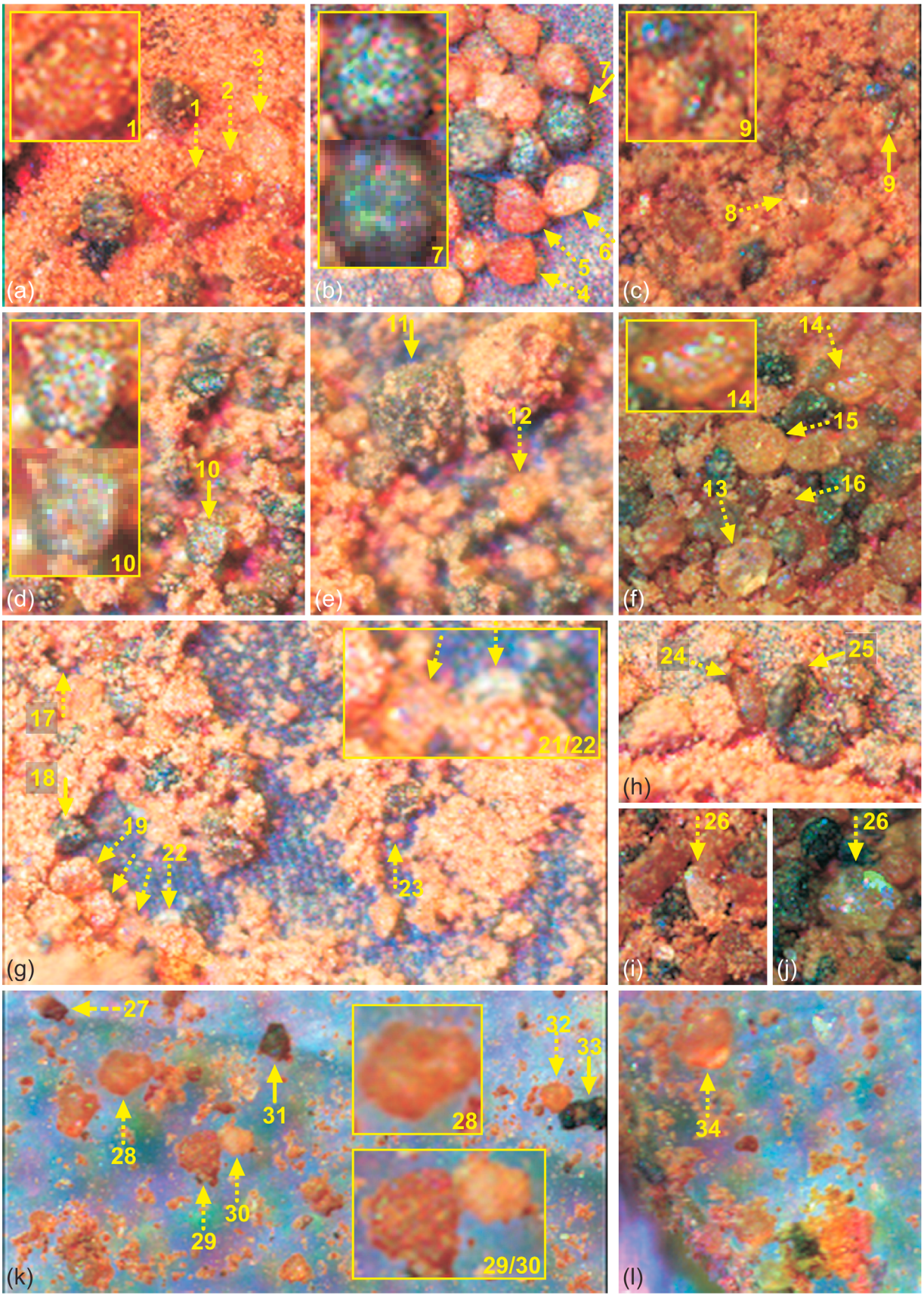
(a)
1
2
3
(b)
7
4
5
6
(c)
9
8
(d)
10
(e)
11
12
(f)
14
15
13
16
(g)
17
18
19
22
23
21/22
(h)
24
25
(i)
26
(j)
26
(k)
27
28
29
30
31
32
33
29/30
(l)
34

Figure 6

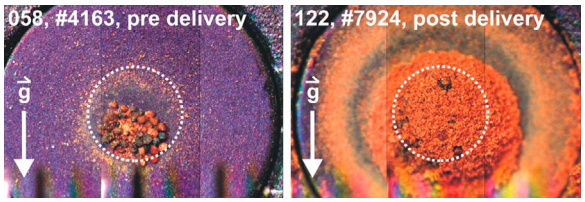

Figure 7. Interaction of Phoenix soil particles with permanent magnets. The same substrate (circular, 3 mm in diameter) is shown before and after soil delivery. Particles that have previously been delivered to a given substrate can potentially move later on to another substrate due to excitation caused by the motion of the sample wheel. This explains why some particles had already settled on the substrate (left) prior to soil delivery. When recording OM images the substrates are oriented vertically with the gravity vector g pointing downward. All particles are noticeably magnetized, as they stick to the near center of the substrate. The permanent magnet (cylindrical, 1 mm in diameter, 1.8 mm thick) is located 0.2 mm below the substrate surface [*Leer et al.*, 2008]. Its position is indicated by the white dotted line in both images.

a thin weathering rind. Whenever that rind is incomplete, reflecting facets from the particle's interior would become visible and could explain the above mentioned bright glints of black sand particles. However, the existence of such a weathering rind remains uncertain, as its thickness would not exceed two pixels. As a result that weathering rind represents a potential feature at the limit of the OM resolution.

[33] We now consider the brown sand particles. An important property is their diversity in color, size, shape and texture. The color of these particles varies from transparent to dark brown (opaque) (see particles 1–6, 8, 12, 13–17, 19–24, 26–30, 32, 34), although most of them are translucent to some degree (see, e.g., particles 2, 4, 12, 14, 34, in addition to the almost transparent particles referred to below). Their surfaces do also show glints just like the black particles (see the above discussion). However, these glints (see inset in Figure 6f) have a different appearance than those from the black particles (see insets in Figures 6c–6d). In particular, the glints from the brown sand particles extend over a larger (several pixels wide) area as a result of the surface smoothness of these particles. Some brown sand category particles are almost transparent (see particles 3, 6, 8, 13, 22, 26), which rises again the question of their affiliation to that particle type.

[34] The size of brown sand particles varies considerably: The oval, shiny particles 17 and 23 have a major diameter of less than 30 μm, whereas others (e.g., particles 19–20) are in the range 60–80 μm. Particle 26 (shown at two different orientations, Figure 6i–6j) has a major diameter of 130 μm. Brown particles can have any shape from angular (particles 13, 16, 21–22) to subrounded (e.g., particles 19–20). Their texture is diverse (compare, e.g., particles 1–2, 28–30 to each other) with particles 1, 29, and 30 having lineated surface textures. These features are unlikely to be caused by image compression artifacts, as they do not show up in otherwise comparable regions of the same images.

[35] Figures 6k–6l show material on the silicone substrate. This substrate exhibits reflection from the machined aluminum stub on which the silicone is mounted, thus providing weak additional illumination of particles from below. The artificial colors of Martian material in the lower part of Figure 6l show that illumination from below (next to the dominant one from above) is significant on these types of substrates. Therefore the differences between translucent particles may also represent differences in their internal structure. As a result the above mentioned lineated surface texture of particles 29/30 (as opposed to particles 28/34) may actually be a three-dimensional feature implying a layered (internal) structure.

[36] The amount of ferric iron has been used as a sensitive marker for geochemical alteration and formation of secondary (iron bearing) phases [e.g., *Morris et al.*, 2006a, 2006b, 2008]. In our case the brownish color of the brown sand category of particles can be ascribed with some confidence to a higher content in ferric iron indicating that these particles are more (chemically) weathered than the black ones. Their susceptibility to weathering should be the key to that diversity: brown sand particles break more easily and are subjected to faster chemical weathering than black ones. Their diversity would then be caused by the fact that they have reached different stages of their breakdown and alteration. This should be a plausible, though preliminary explanation of the observed diversity in terms of color, size, shape, and surface texture. Further studies on terrestrial analog soils will be needed in order to confirm this interpretation. However, at the present stage, there is no clear rationale for defining further subclasses for this particle type.

3.3. Magnetic Properties of Soil Particles

[37] One third of all OM substrates have a permanent magnet mounted below the substrate surface. By choosing the size and precise location of the magnet beneath the surface, two substrate types having different magnetic strengths ("weak magnet" and "strong magnet") were fabricated [*Leer et al.*, 2008]. The interaction of Phoenix soil particles with these substrates provides information on the magnetic properties (magnetic susceptibility and saturation magnetization) of the soil particles. Figure 7 shows the same substrate before and after delivery of the soil Mother Goose (delivery on sol 67). The substrates are oriented vertically with respect to the local surface on Mars. The particles stick to the substrate surface, slightly below its center, attesting to a substantial magnetization of the particles. To a first approximation all particles (both the sand-sized grains and the particles making up the red fines) appear to be magnetized in a similar way.

[38] Figure 8 shows the two end-members of through focus imaging of the strong magnet on sol 31. Given that the sample wheel has been moved by 225 μm toward the OM between the acquisition of these two images, and given a depth of focus of 50 μm, we infer the pile height to be of the order of ~300 μm, which is a typical value for Phoenix soil materials that accumulated and were held on the strong magnet over the course of the mission. Comparison with preflight simulation experiments [*Leer et al.*, 2008] shows that the saturation magnetization of Phoenix soils is in the range 0.5 to 2 A m^2 kg^{-1}. This result is close to previous inferences of the magnetization of soils [*Goetz et al.*, 2008a, and references therein] and rocks [*Morris et al.*, 2006a; *Goetz et al.*, 2008b].

[1]Animations are available in the HTML.

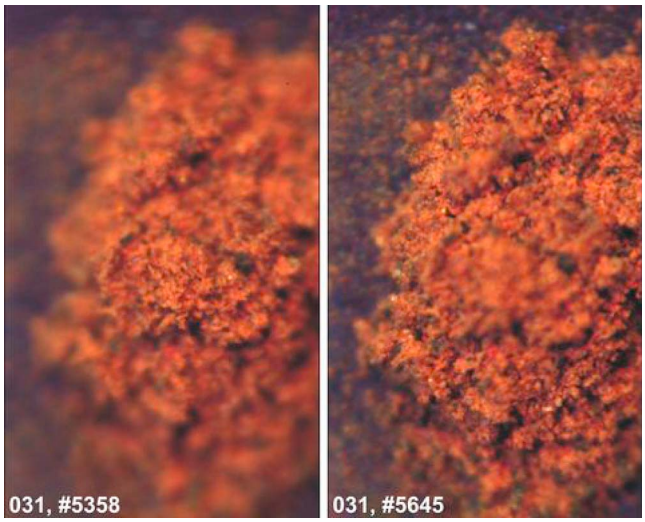

Figure 8. Material pile on the strong magnet: The two end-members of a through focus series of four images (sol 31, 5358, 5454, 5549, 5645). Both images shown are 1 mm wide (256 raw pixels). (left) Only the central top part of the pile is in focus. (right) The substrate surface is nearly in focus. The depth of field is 50 μm and the sample wheel has been moved by 225 μm (900 steps) toward the OM in between the acquisition of these images. These numbers imply a pile height of ~300 μm, a rather common value for Phoenix soil material collected on the strong magnet.

[39] Figure 9 shows the motion of brown sand-sized particles on the strong magnet (sol 123) as a result of sample wheel motion (See Animation 1).[1] Apparently the brownish particles are more loosely bound to the substrate by magnetic forces than the nearby black particles (white arrow). We interpret this observation as an indication for a lower magnetization of the brownish particles (brown sand) as compared to the black ones (black sand). An alternative interpretation would be that the specific black sand particle in Figure 9 was accidentally more efficiently immobilized by surrounding fines and sand.

3.4. Size Distribution of Soil Particles

[40] This section presents size histograms of Phoenix sand grains. Further analysis of the red fines and a model for the production of Phoenix-like soil particles as inferred from both OM images and AFM data will be discussed by W. T. Pike et al. (manuscript in preparation, 2010).

[41] The size distribution beyond 200 μm cannot be inferred from OM images because larger particles are physically restricted from entering the OM. Figure 10 shows RAC images that are used for the study of particles larger than ~200 μm. Figures 10b and 10d show millimeter-sized particles near the bottom and on top of the Thermal and Evolved Gas Analyzer (TEGA). These particles are interpreted to be soil agglomerates that either were not disrupted, because they fell on soft (previously deposited) soil, or because they formed from much smaller (perhaps silt sized) grains that were rolling over cohesive soil down the oblique side plane of TEGA. In any case, there is no clear indication in these images that these millimeter-sized "particles" represent

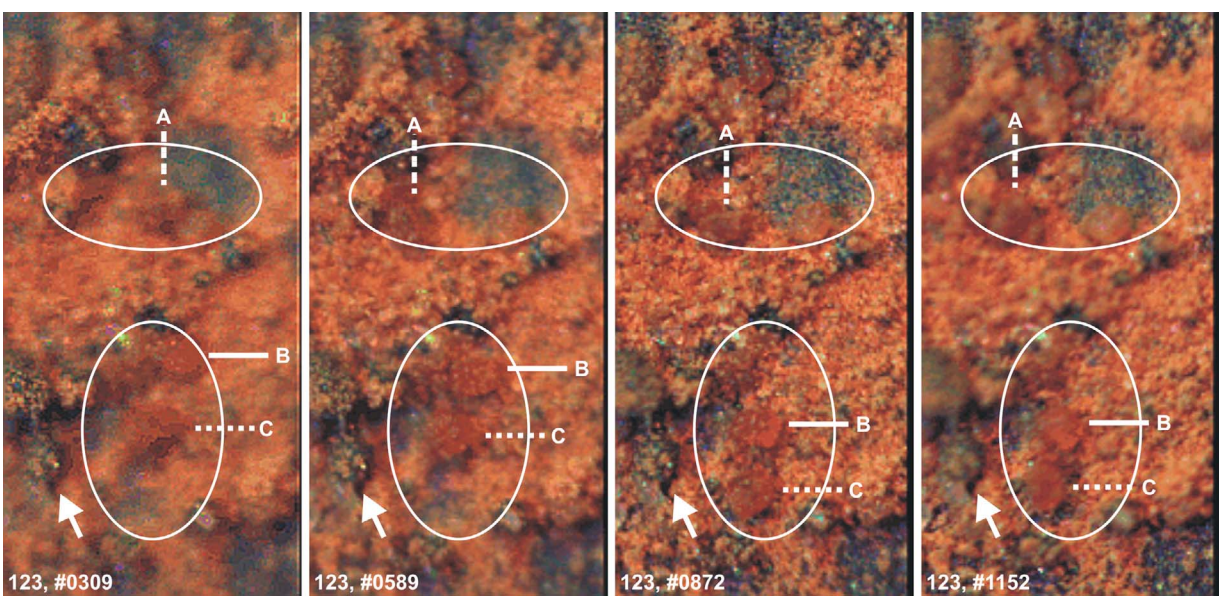

Figure 9. Motion of brown sand grains on the strong magnet (sol 123). Each image is 0.5 mm (128 raw pixels) wide. The four images were acquired within about 800 s as indicated by the image identifiers. Ellipses and arrows serve as positional reference in each image; they are placed at the same relative location with respect to the substrate. Sample wheel motions between image acquisitions caused brown grains to move around within these ellipses. The varying position of three particular grains (labeled by A, B, and C) is marked by 100 μm long bars. Note that the black grains (white arrows) do not seem to move, suggesting that these grains are more strongly magnetized than the brown ones. Animation available in the HTML.

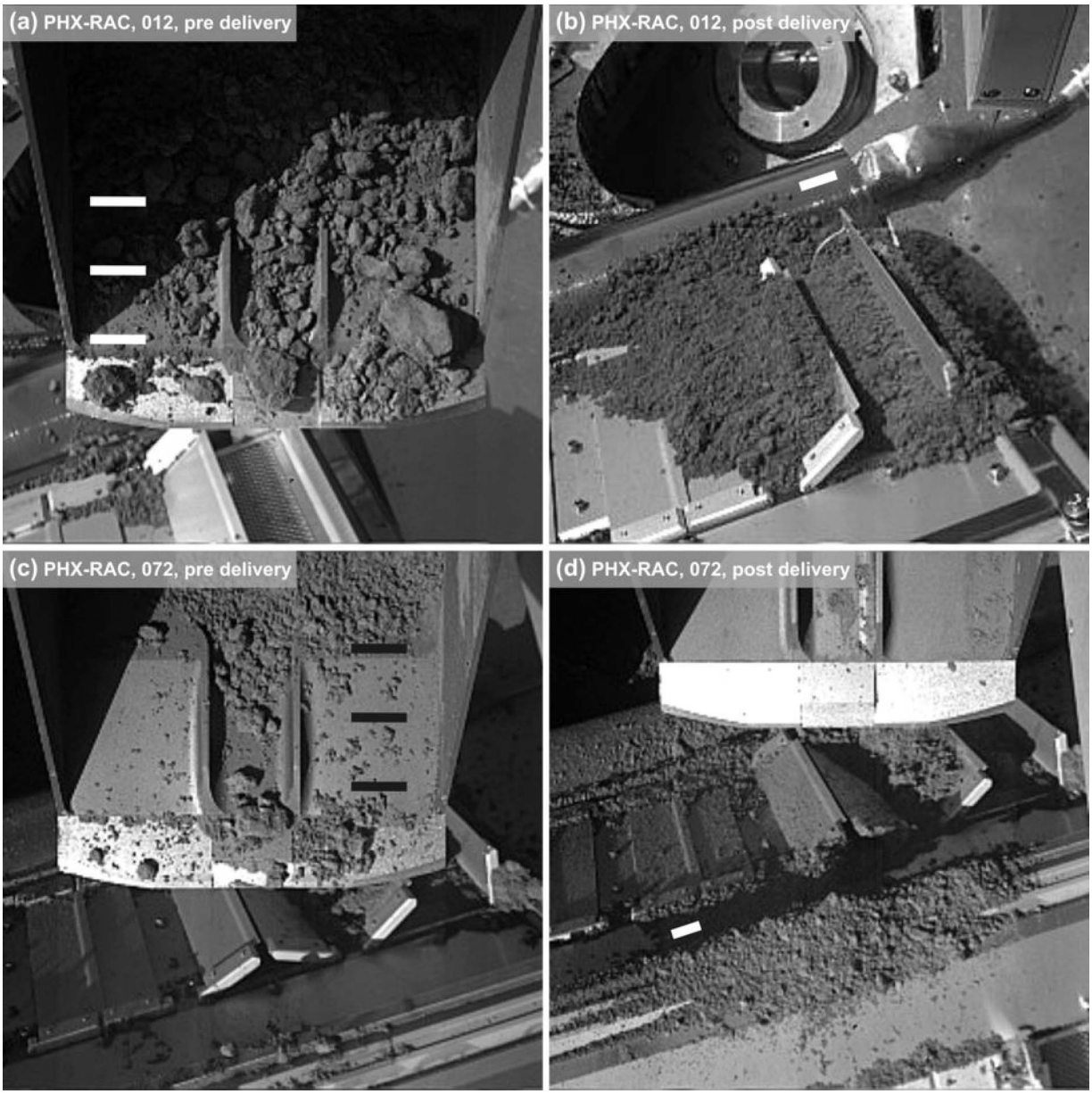

Figure 10. (a and b) Delivery (sol 12) of the sample Baby Bear to the Thermal and Evolved Gas Analyzer (TEGA), cell 4. (c and d) Delivery (sol 72) of the sample Rosy Red to TEGA, cell 5. The scale bars shown at different locations measure 10 mm at the target. Figures 10 and 10c are predelivery of soil, and Figures 10b and 10d are post delivery of soil. The delivery was achieved by "sprinkling" (conferring vibrations to the scoop by actuating the icy soil acquisition device). Millimeter-sized rounded clods can be seen near the bottom (Figure 10b) and on the top part of TEGA (Figure 10d).

mechanically stable sand grains. Figure 11 shows particles from Golden Key soil as imaged by RAC (scoop load prior to delivery to OM) and OM. Sand-sized dark particles (black sand) can be identified in both RAC and OM images. Moreover the relative abundance of these particles appears to be similar in both types of images indicating little sampling bias in the case of the OM images. It is also estimated that the fines are cohesive enough to hold potential larger (sand sized) grains in the divot location of the scoop [*Arvidson et al.*, 2009], if such grains were present in the soil. The absence of larger (sand sized) grains in the RAC divot image (Figure 11a) is interpreted to indicate the absence of such grains in the corresponding scoop load, and most likely in other Phoenix soil samples as well.

[42] Figure 12 shows cumulated size distributions of black and brown particles that are believed to be a representative subset of Phoenix soil grains. Each diameter that enters these histograms is the average of the short and long diameter of a particular grain. The grains were selected by hand. Among the selected grains black and brown ones had very similar size, therefore the histograms for both particle types were merged. The hand selection of the grains may have caused a bias toward the larger (easier recognized) grains and a corresponding bias in the resulting size distributions. All

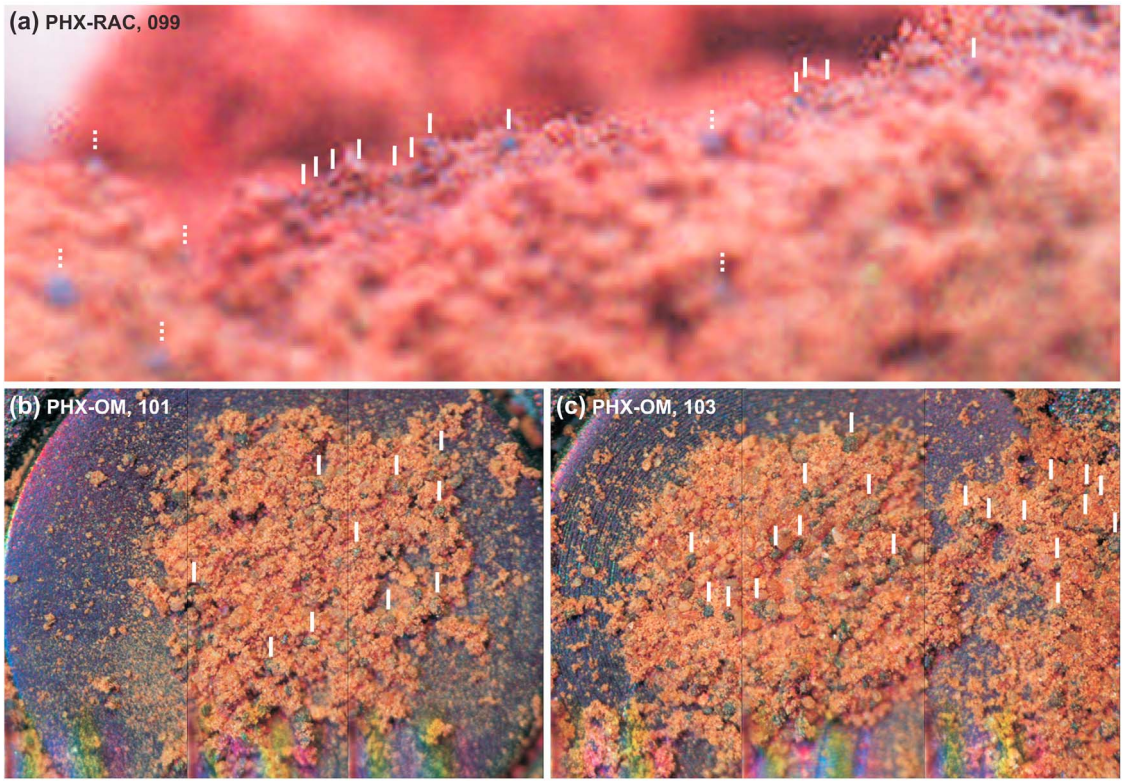

Figure 11. Particles from Golden Key soil as imaged by OM and RAC. (a) RAC divot image (sol 99, 6504, false color), about 6 mm wide in the region of best focus. The prominent silt- to sand-sized particles belong to the black sand category but appear bluish in this color stretch. They are marked by a white line placed above the corresponding particle. Solid and dotted lines mark particles at and in front of the region of best focus, respectively. Therefore, the latter (blurry) particles appear somewhat larger. The brown sand particles cannot be distinguished in RAC divot images. (b) OM pseudo true color image (sol 101, 5738, 5830, and 6207) of the weak magnet postdelivery of the soil sample. (c) As in Figure 11b, but of the strong magnet (sol 103, 6251, 6438, and 6622). Note that large amounts of soil material adhere to the surface of the sample wheel outside the area of the circular substrate, attesting to the stickiness of the soil. In Figures 11b and 11c prominent (black) particles are marked by white bars placed above the corresponding particle (as in Figure 11a). Figures 11a–11c are all at the same scale. The circular substrates visible in Figures 11b and 11c are 3 mm in diameter. Figures 11a–11c suggest that the black sand particles appear in similar abundance and size in OM and RAC images. This indicates little or no sampling bias in the case of the OM.

histograms taken together have a number maximum and a volume-weighted maximum at a particle size of 53 and 66 μm, respectively. Figure 13 compares these size distributions to those of wind ripples at Gusev crater. A rather complete study of Gusev soils in terms of particle size distributions can be found in [*Cabrol et al.*, 2008]. The Phoenix-OM images shown in Figure 13 are 1 mm (sol 21 and 58) and 2 mm (sol 103) wide. The MER-A images (32 mm wide) show two different types of ripples cut off by the rover wheel: a ripple in the Columbia Hills (A707, "El Dorado"), and another one on the Gusev plains (A073, "Serpent"). These two ripple types are referred to as ordinary and coarse-grained ripples, respectively, and are believed to be widespread on Mars [*Sullivan et al.*, 2008]. Thus it is conceivable that particles from these ripple types are found at the Phoenix landing site. The particle size distribution for the Gusev wind ripples (number maximum at ~90 μm in the ripples' interior) is offset to higher values compared to Phoenix soils, although the difference may be an artifact resulting from the higher spatial resolution of Phoenix OM compared to MER MI.

[43] Figure 14 shows size distributions of Phoenix soil (same as in Figure 13) and MER-A airborne particles that were accumulated on the rover deck [*Landis et al.*, 2006] and on the magnets. The MER-A images show sand-sized particles on the magnets and on the deck that are occasionally

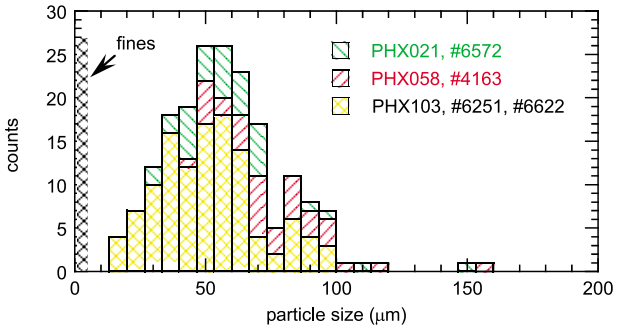

Figure 12. Cumulated size distributions of black and brown sand-sized particles.

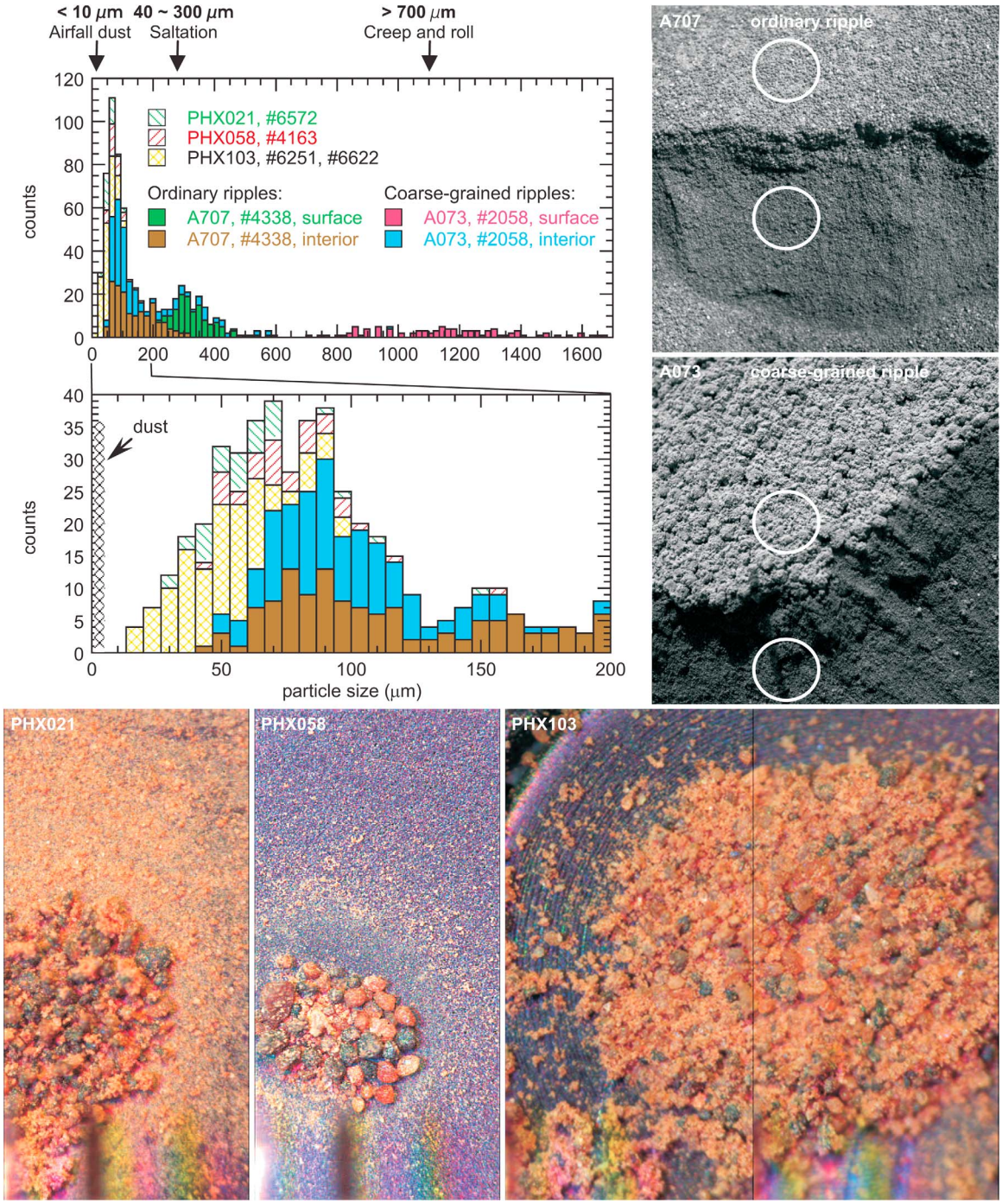

Figure 13. Size distributions of Phoenix soil and MER-A ripple particles. The hatched and filled histogram bars refer to Phoenix-OM and MER-MI images, respectively. The size distributions are not normalized. Bin width of top and bottom histogram is ~19 μm and 7 μm, respectively. The presumed mode of transport for different particle size ranges is specified on top. The Phoenix-OM pseudo true color images are 1 mm (sol 21 and 58) and 2 mm (sol 103) wide. The MER-A images (32 mm wide) show two different types of ripples cut off by the rover wheel: An ordinary ripple (A707, "El Dorado") and a coarse-grained one (A073, "Serpent"). The particle size distribution up to 200 μm appears to be shifted to smaller values for Phoenix particles as compared to Gusev particles. However, this may be an artifact due to the different resolution of the instruments involved (OM for PHX, MI for MER-A). Particles in the size range 500–700 μm are rare in Gusev soils. Phoenix soils apparently exhibit a lack of medium to large sand grains (200–1000 μm).

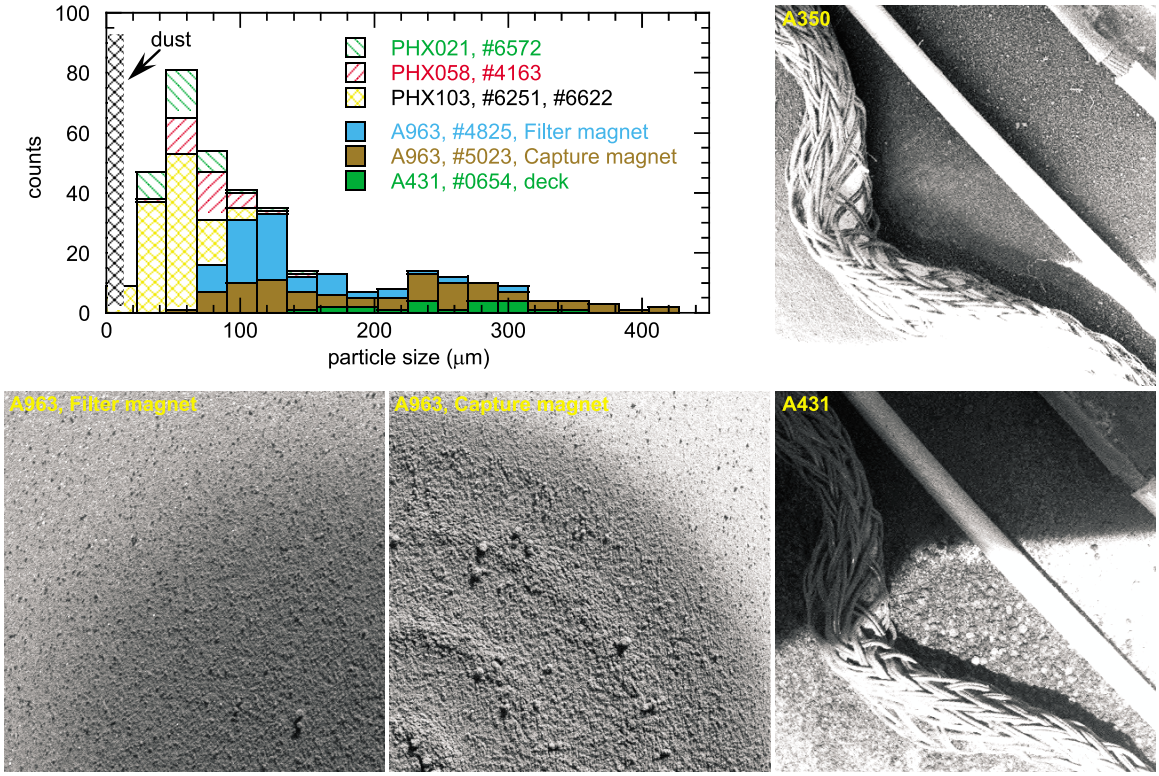

Figure 14. Size distributions of Phoenix soil (same as in Figure 13) and MER-A airborne particles that accumulated on the rover deck and magnets. The MER-A images (13.4 mm wide, 430 × 430 pixel crops) show sand-sized particles on the magnets (upper left/right quadrant of filter/capture magnet; image 4825 and 5023) and on the deck (image 7650 and 0654) which have occasionally been kicked up by events of strong wind.

kicked up by events of strong wind. Figure 14 demonstrates that 100 to 300 μm large particles are moved around by saltation in the present-day Martian environment and can in exceptional cases be moved up to about one meter above the surface. These types of particles appear to be absent in Phoenix soils. Particles in the size range 500–700 μm are generally rare in Gusev soils including the wind ripples discussed here [*Sullivan et al.*, 2008], and also these types of particles are not clearly identified in Phoenix soils.

[44] We conclude that Phoenix soils may indeed lack sand-sized particles in the range from 200 μm to about one millimeter. This result is based on RAC and OM images and is consistent with the lack of sand ripples and dunes at the Phoenix landing site as documented by SSI images. Particles that are several millimeter in size though have been observed on the lander deck as reported by [*Leer et al.*, 2009].

3.5. Phoenix Soil Particles in Context: Comparison to MER, MRO, and Hubble Data

[45] The goal of this section is to compare the optical properties of Phoenix soil particles (section 3.1) to a variety of different data sets including MI data of El Dorado ripples in Gusev crater, SSI spectra of dust on the magnets, CRISM spectra of the Phoenix landing site area, and WFPC-2 spectra of high-altitude atmospheric dust.

[46] Figure 15 shows sand-sized particles of different albedo at the MER-A and Phoenix landing sites. The high-resolution MER-MI image shows the bottom of a trench near the border of the El Dorado dune field (Figures 15a–15b). It has been acquired in deep shadow implying that the imaged soil is illuminated by diffuse reddish skylight. Therefore it may be compared to red Phoenix-OM images (Figures 15c and 15e). The OM and MI images (Figures 15b–15f) are all at the same scale. Dotted and solid arrows point to bright and dark particles, respectively. The El Dorado particles are somewhat larger (200–300 μm) than the Phoenix ones (50–100 μm). However, smaller particles are known to be abundant (if not dominant) in the El Dorado dunes, but are not shown here, as they are not well resolved in MI images.

[47] In the red image from Phoenix, sol 58 (Figure 15c), the top (*black sand*, solid arrow), middle (*bright brown sand*, dotted arrow), and bottom particle (*brown sand*, dashed arrow) have a relative brightness of 1.0 (by definition), 3~4 and 2~3, respectively. Similarly, in the red image from sol 123 (Figure 15e), the black particle to the right (solid arrow) is a factor of 2~4 darker than the brown ones (dotted arrows). Thus the red albedo of Phoenix silt- and sand-sized grains varies by a factor of more than three. The brightness of El Dorado particles as inferred from MI shadow images (Figure 15b) varies within only a factor of two. However, instrumental and observational circumstances tend to lower the brightness range of El Dorado particles as inferred from these images: (1) Although El Dorado is known to be a fairly dust-free region [*Sullivan et al.*, 2008], a thin dust veil cannot be excluded either and would tend to lower the observed brightness range between the different dune particles.

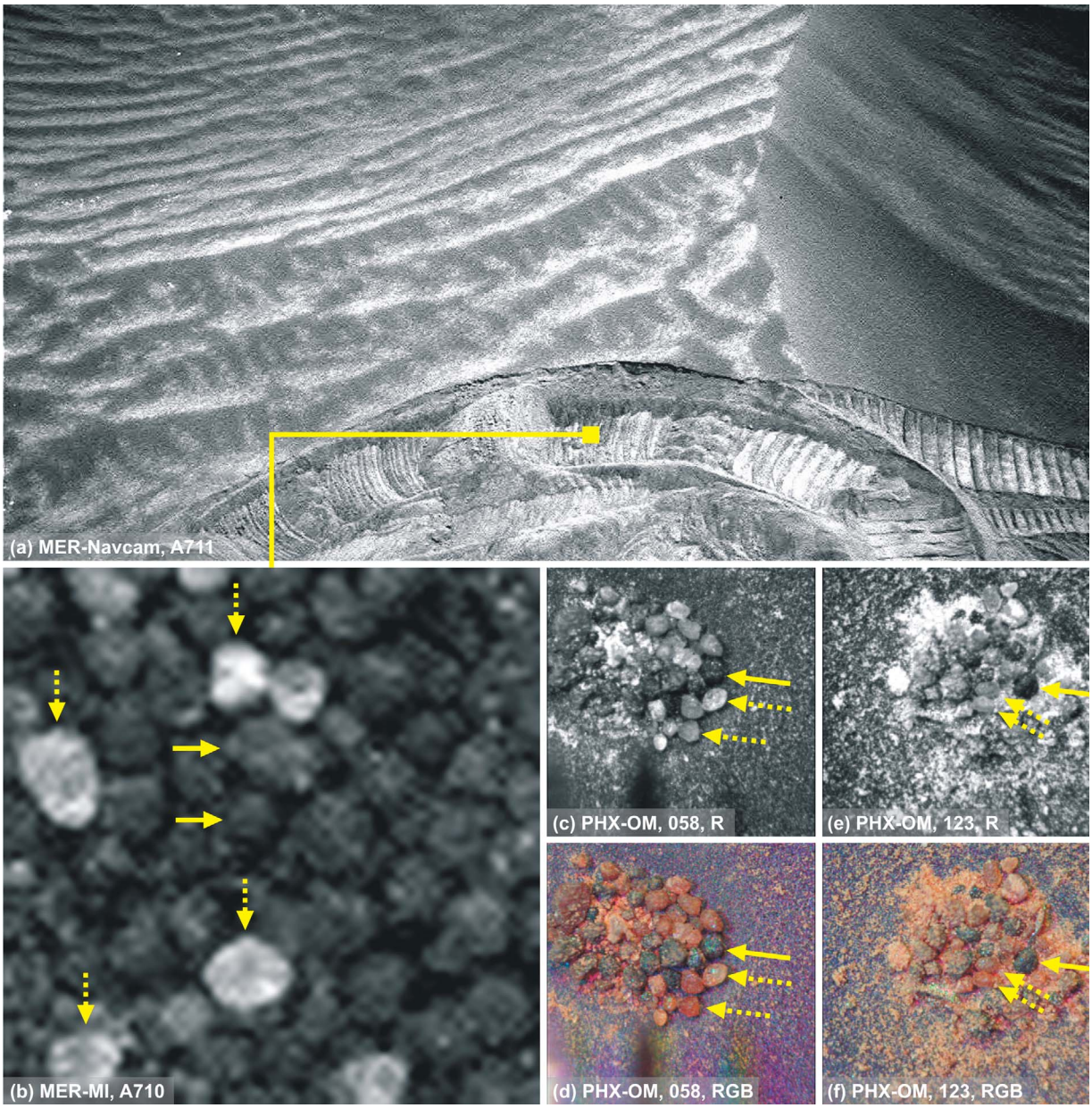

Figure 15. Sand-sized particles of different albedo at Gusev crater (El Dorado dune field) and at the Phoenix landing site. (a) Navigation camera (Navcam) image, sol A711, image 2856. The wheel tracks in the foreground give a sense of scale (each wheel is about 16 cm wide). This image provides the context for Figure 15b. (b) Detail (64 × 64 pixels) from MI image (sol 710, image 3476). (c–f) Phoenix OM images (sol 58, image 4163; sol 123, image 2410). All high-resolution images (Figures 15b–15f) are at the same scale. The Phoenix OM images (Figures 15c–15f) are 1 mm wide. Solid and dotted arrows point to dark and bright particles, respectively. The bright MI particles in Figure 15b display strong albedo variations within each particle that are attributed to varying bulk optical properties. The regular (hatched) pattern on these particles is a compression artifact.

(2) Differences in brightness must be smaller in the blue part than in the red part of the spectrum. Thus, the observed brightness range of these dune particles is lowered due to the broadband character of the MI. More specifically, the signal in MI shadow images is equal to the convolution of the photon flux from the Martian sky [see, e.g., *Maki et al.*, 1999], the reflectance of the particle in question and the broadband responsivity of the camera CCD (particularly in the spectral range from $\lambda = 500$ nm to 650 nm, [*Herkenhoff et al.*, 2003]). To the contrary, red OM images are acquired in (largely) monochromatic light (center wavelength ~630 nm, with a full width at half maximum of ~20 nm, [*Hecht et al.*, 2008; *Keller et al.*, 2008]) and can therefore be directly interpreted in terms of particle albedo at that particular wavelength.

[48] Given the above described uncertainties the actual brightness range of Phoenix soil grains and Gusev/El Dorado dune particles may not be as different from each other, as a quick analysis of these images may suggest. Note that the

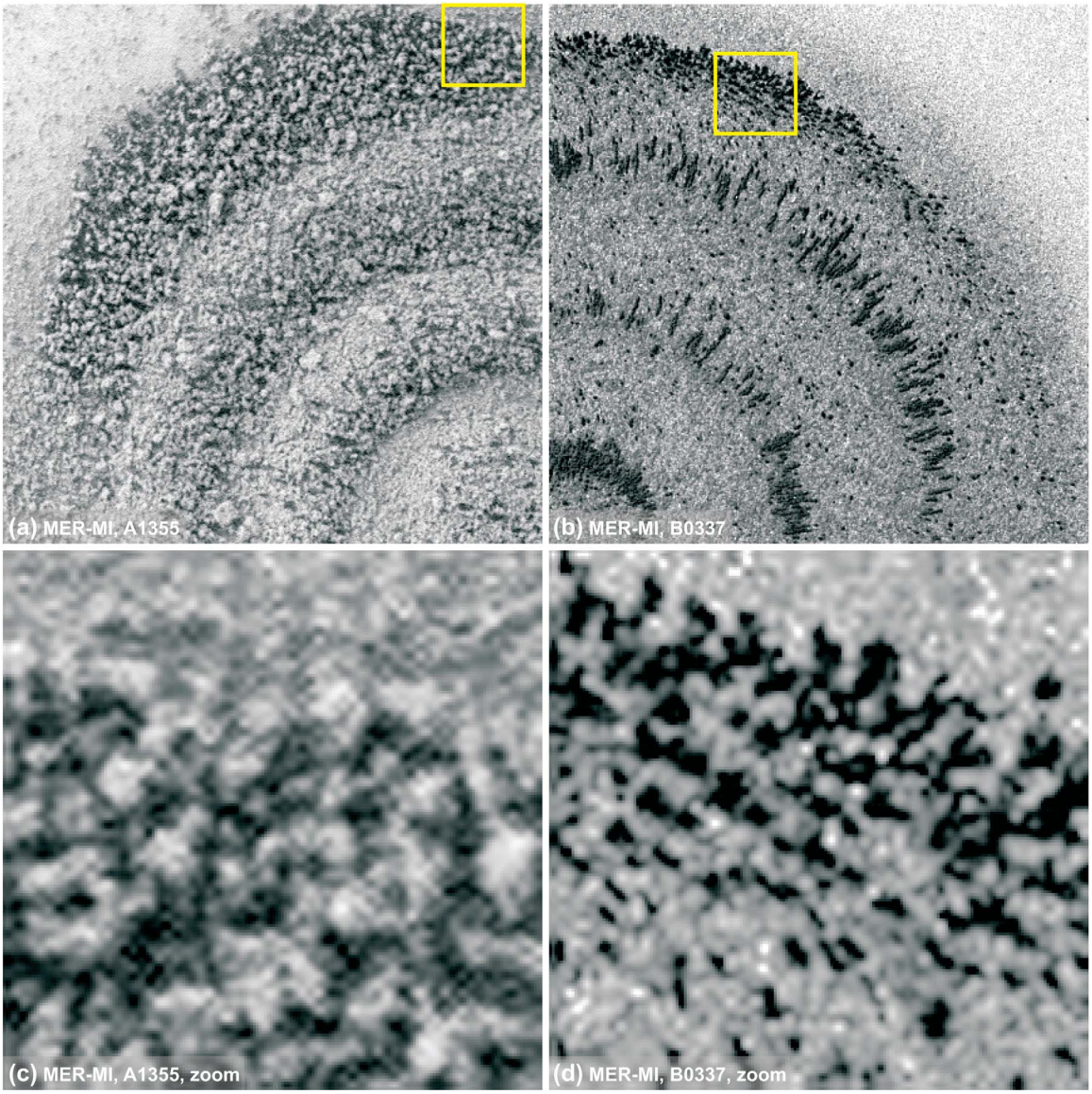

Figure 16. Particles of different albedo on the capture magnet onboard MER-A and MER-B. (a) A1355, MI image 1970, top left quarter of the capture magnet. (b) B0337, MI image 9569, top right quarter of the capture magnet. (c) Zoom of Figure 16a. (d) Zoom of Figure 16b. The sharp bright spots in Figure 16d are reflections from the substrate and do not represent Martian particles. Figures 16a and 16b are about 15 mm across. Figures 16c and 16d are about 2 mm wide and are at the same scale as Figures 15b–15f.

bright particles in the OM and MI images (Figures 15b–15f) have shiny areas. Thus their brightness does not only vary from particle to particle, but also varies within each particle. Glints in OM images are likely caused by specular reflections. However, in the case of MI shadow images these shiny patches show up at uniform (diffuse) illumination and are therefore more likely caused by varying absorption or light scattering across the bulk of the translucent grain rather than specular reflection and surface topography.

[49] Figures 16a and 16b show windblown material (presumably all kinds of aeolian particles from dust to sand sized) on the capture magnet surface [*Madsen et al.*, 2003, 2009] as of sol A1355 and B0337, respectively. The images demonstrate the large variation in particles that can be accumulated on these surfaces under different atmospheric opacity and wind conditions. Figures 16c and 16d show zooms of Figures 16a and 16b, respectively. These zooms are 2 mm wide, and thus are at the same scale as PHX-OM and MER-MI images in Figures 15b–15f. In particular Figure 16c shows a zoom of the very border of the windblown material layer that has a pronounced bimodal albedo: Dark patches alternate with bright ones at a characteristic spatial frequency across the surface of the magnet and have a relative brightness of 1.0 and 1.2 ~ 1.4, respectively. The brightness variation as observed on the A1355 capture magnet (Figure 16a and 16c) is thus lower than that observed in the soil on A710 (Figure 15b). This may be caused by the fact that the material on the capture magnet and the dune soil represent two different subsets (size fractions in particular)

of Martian surface material with varying admixture of air fall dust.

[50] Figures 16b and 16d show very dark particles that did resist events of strong wind as a result of their strong magnetic attraction to the capture magnet surface. Data from the Alpha Particle X-Ray Spectrometer (APXS) and from the Mössbauer spectrometer of precisely that material pointed to a high abundance of black (pigmenting) titanomagnetite in these particles [*Goetz et al.*, 2005; *Madsen et al.*, 2009]. Based on these results and given that the black sand particles appear to be the most strongly magnetic components in the Phoenix soils (section 3.3), we expect the magnetization of these particles to be caused by magnetite or titanomagnetite as well.

[51] Overall we conclude that silt- to sand-sized grains with very different albedo exist at both landing sites (Phoenix, MER-A). The grains have similar morphology. Their red albedo range appears to be wider at the Phoenix site (1 ~ 4) than at Gusev/El Dorado (1 ~ 2), although observational biases may not have been fully assessed.

[52] The El Dorado dune particles are well resolved by the MI, so the above statement on the existence of such particles is firm. However, the El Dorado dune field is a rather particular place in Gusev crater with a particularly mafic chemistry and mineralogy [*Ming et al.*, 2008; *Morris et al.*, 2008]. The magnet surfaces on both rovers also show bimodal albedos, although the albedo range is even smaller and refers to a characteristic sample of windblown near-surface material.

[53] In Figure 17 VIS/NIR reflectance spectra of OM dust are compared to spectra for other dust units or relevant surface areas. The dust units chosen for comparison are dust on the magnets as imaged by the SSI [*Drube et al.*, 2009] and high-altitude airborne dust as imaged during a global dust storm (4 September 2001) by the Wide Field Planetary Camera-2 (WFPC-2) onboard the Hubble Space Telescope (HST). The surface areas that were selected for the present study are bright (dusty) and dark (largely dust-free) areas in Gusev crater as well as the near surroundings of the Phoenix landing site that were targeted by CRISM. The acquired spectra (Clark Hill, El Dorado) shown in Figure 17 are from *Arvidson et al.* [2008].

[54] When comparing the SSI spectrum of dust on one of the magnets to the Earth-based (HST/WFPC-2) reflectance spectrum of the Martian disk during a global dust storm, we may (or may not) refer to the same material. On the magnet the dust is somehow compacted, while in the WFPC-2 spectra the dust is "diluted" implying that diffraction plays a stronger role [*Hapke*, 1993]. The SSI spectra were corrected in the sense that diffuse surface illumination from the Martian sky has been removed during calibration. In other words the SSI image calibration pipeline transforms the (directly measurable) combined hemispherical directional and bidirectional reflectance into a pure bidirectional reflectance, which facilitates comparison with reflectance data acquired in the laboratory. The WFPC-2 spectra have, of course, not been corrected for diffuse illumination from the sky. Such a correction would not make sense, as the target of that observation is not the Martian surface but the layer of airborne dust that was, at the time of observation, almost semi-infinite from an optical point of view. In addition we measure the reflectance "from far away" implying perfect bidirectional geometry. The major difference is that the light returned from the dusty Martian atmosphere back into the detector of the camera has penetrated the Martian atmosphere deeply (partially hitting the surface, as documented by the weak surface features that are still distinguishable in the NIR images). When comparing CRISM spectra to WFPC-2 spectra we should remember that we are comparing spectra of selected surface areas (CRISM) to the spectrum of diluted (suspended) airborne dust (WFPC-2). In other words the CRISM spectra have been acquired during periods of relatively low atmospheric dust loading (low in comparison to the WFPC-2 spectra), and the spectral effect due to secondary illumination from the Martian sky has been removed. The result is a state-of-art bidirectional reflectance spectrum of a well-defined area on the surface of Mars. The WFPC-2 spectra are unrecoverable from that point of view. Thus in these spectra we accept some (blurry) surface features shining through as an inherent error in these spectra. Finally a brief note on the OM spectra presented: As outlined in section 3.1.1 we defined a ROI "all" for the mixed material on the strong magnets. Within that ROI we defined smaller ROIs that were dominated by a certain component of that material. The average spectrum of the ROI "all" can thus be described as a linear combination (also referred to as an areal mixture) of the component subspectra. The areal mixture model is perfectly valid in this case and is not challenged by the well-known nonlinearity of intimate mineral mixtures in terms of their reflectance spectra. In the remainder of the present section the reflectance spectra in Figure 17 will be compared to each other with the above outlined caveats in mind.

[55] The area selected in the WFPC-2 image (20° × 20°, centered on 15°N, 330°E, SE Arabia Terra) should be among the dustiest on the planet (as demonstrated by its very low thermal inertia [*Putzig and Mellon*, 2007]). As a result, no surface features can be distinguished in this area, neither in the blue region (Figure 17c) nor in the NIR (Figure 17d). It can be seen that higher-altitude airborne dust during the planet-encircling global dust storm in September 2001 has the brightest reflectance. Airborne dust as accumulated on the medium gray magnet target on the Phoenix deck (arrow in Figure 17b) [*Leer et al.*, 2008; *Drube et al.*, 2009] has a somewhat lower albedo and a clearly different spectral shape. These differences are likely caused by a variation of both grain size and mineralogy as a function of altitude [*Goetz et al.*, 2009]. The reflectance of "all" OM material (i.e., particles in the ROI "all," see Figure 2b) is similar to the CRISM spectrum of the landing site within the uncertainty. Moreover the reflectance spectra of "all" OM material is also consistent with that of a typical soil patch at the Phoenix landing site as imaged by the SSI. The red fines in the OM image are only marginally brighter and cannot reach the brightness of dust on the magnet. We conclude that some difference persists between pure airborne dust (as accumulated on the magnet) and "dusty" material observed by the OM.

[56] The spectra of different OM subgroups (red fines, brown sand, and black sand) are also plotted in Figure 17. In particular black sand and brown sand taken together and in the right proportion could have a spectrum that would be consistent with the CRISM El Dorado data.

[57] One notices that the difference between the OM reflectance of "all" material and red fines (at $\lambda = 630$ nm) is similar to the difference between the Phoenix landing site and the Clark Hill CRISM spectra (in the red/NIR spectral region). Assuming the Phoenix soil to be a mixture of a dark

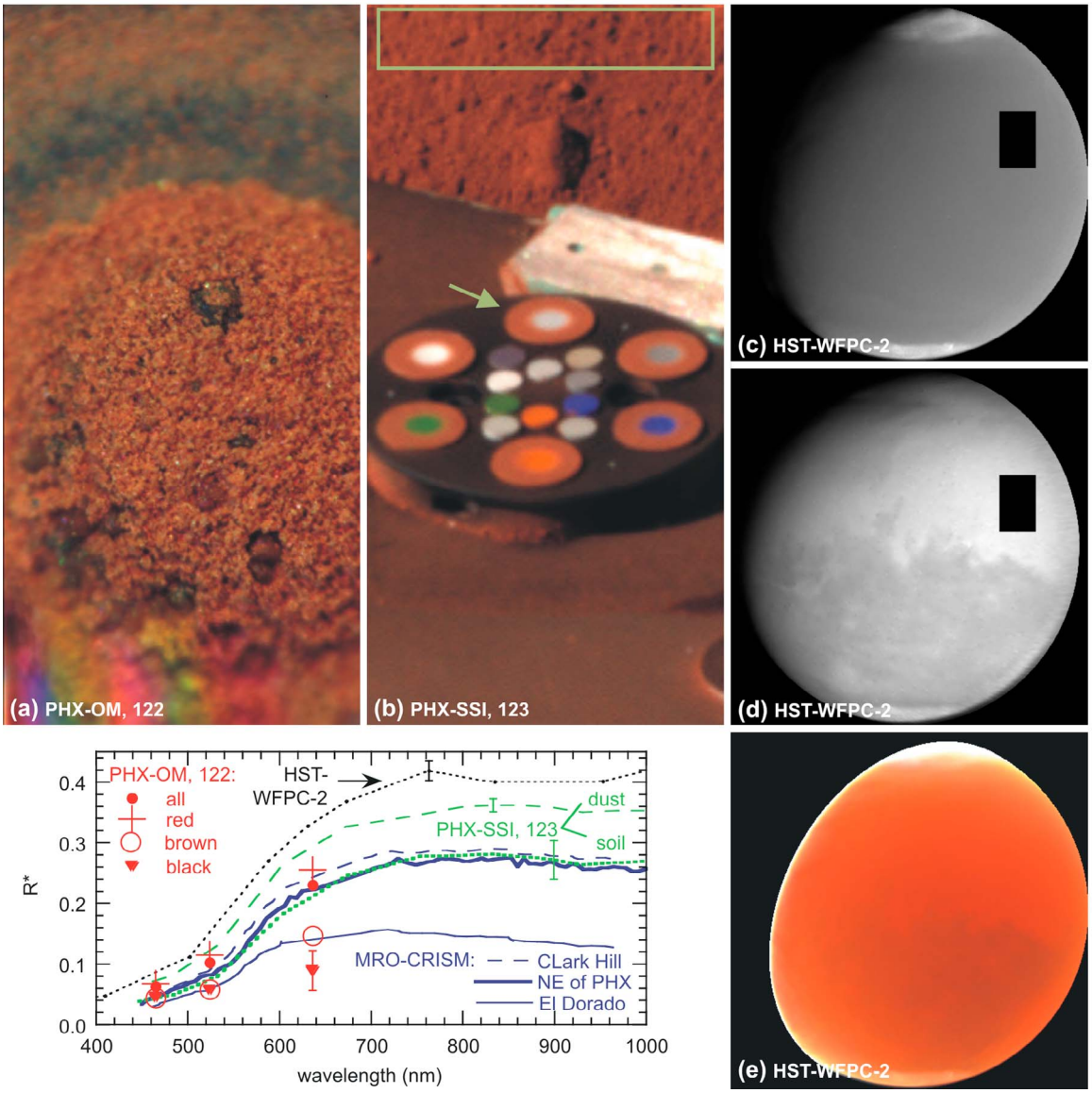

Figure 17. Reflectance spectra in the VIS/NIR region for different Martian samples: (a) OM, sol 122, 7924, pseudo true color composite. The image is 1 mm wide. (b) SSI, sol 123, 9288, pseudo true color composite. The green arrow specifies the magnet (medium gray magnet) for which the spectrum of accumulated dust is shown. The green rectangle specifies the region of interest used for the SSI soil spectrum. Scale: The SSI radiometric calibration target in the foreground is 52 mm in diameter [*Leer et al.*, 2008]. (c–e) Wide Field Planetary Camera-2 (WFPC-2), Hubble Space Telescope (HST) images: Mars during a global dust storm. Images acquired on 4 September 2001. Figures 17c and 17d show monochrome images acquired at $\lambda = 410$ nm and 1042 nm, respectively. The black rectangle specifies the area of interest for the reflectance spectrum shown. Figure 17e is a false color image composed of three R* calibrated images (λ = 410, 502, 631 nm, stretched from 0.0 to 0.4). The area selected (20° × 20°, centered on 15°N, 30°E, SE Arabia Terra) should be among the dustiest on the planet (as demonstrated by its very low thermal inertia) [*Putzig and Mellon*, 2007]. Representative error bars are plotted for each instrument. These errors are defined by the standard deviation of pixels in the region of interest. Thus, they are not true errors, but rather they display the brightness heterogeneity within the region of interest. The OM data from sol 122 are the same as those (ROI averages) presented in Figure 3. The reflectance of "all" OM material is similar to the CRISM spectrum of the landing site within the uncertainty. The spectra of different OM subgroups (red fines, brown sand, black sand) are also plotted. In particular black and brown sand taken together and in the right proportion could make up the CRISM El Dorado spectrum. Soil at the landing site (rectangle in Figure 17b) as imaged by the SSI has a reflectance that is very close to the CRISM one referring to a surface patch nearby the lander. CRISM spectra of very bright (dusty) and dark (largely dust-free) areas (Clark Hill and El Dorado, Gusev crater, respectively) are also shown for comparison (taken from *Arvidson et al.* [2008, Figure 2]).

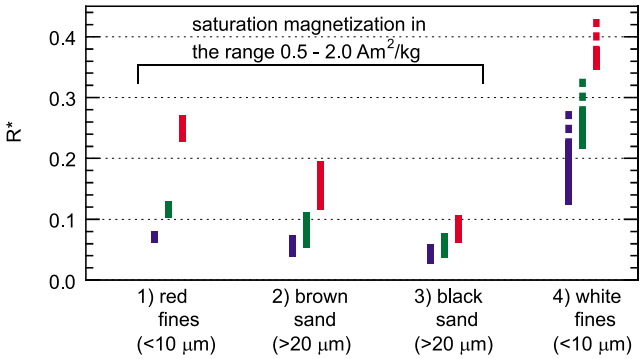

Figure 18. Overview of particle types in Phoenix soils listed in sequence of decreasing abundance (in areal %). The solid bars display the range of average reflectance values (R*) of ROIs as shown in Figure 2c (red fines, brown sand, black sand) and in Figure 5 (white fines as defined by R*(blue) > 0.1, R*(green) > 0.2, R*(red) > R^*_t, see also Table 2). For a given particle type the left, middle, and right bar indicates the reflectance in the blue, green, and red spectral channel, respectively. The reflectance of the white fines as specified is a lower bound (as indicated by the dotted bars). Their actual reflectance depends on contamination by red fines.

and a bright component and applying a simple areal mixing model (checkerboard model) for the overall reflectance of the landing site, Phoenix soils would contain 17% of dark material as inferred from the three CRISM spectra in the red spectral region ($\lambda \sim 690$ nm). A very similar value (18%) is obtained from the red OM data ($\lambda \sim 630$ nm), assuming the "dark" component to be a mixture of brown and black sand particles.

4. Summary and Conclusions

[58] Phoenix-OM images suggest the following classification of soil particles listed in sequence of decreasing abundance (in volume %): (1) red fines, (2) brown sand, (3) black sand, and (4) white fines. Red fines contain both clay- and silt-sized particles. The particle size of white fines is not constrained, but must be smaller than the effective resolution of the instrument (~10 μm). Brown and black sand particles have similar size distributions that range from 20 to 100 μm. The VIS albedo of these materials increases as follows: Black sand < brown sand < red fines < white fines. The relative areal percentage (pixel %) is as follows: white fines $\ll$ black sand < brown sand < red fines. Figure 18 summarizes some of these results.

[59] All Phoenix soil particles (except probably the white fines) are magnetic to some degree. The black sand particles appear to be more strongly magnetic than the brown ones. The saturation magnetization of the bulk soil is in the range 0.5-2 $Am^2\ kg^{-1}$ similar to soils at the Viking landing sites [*Goetz et al.*, 2008a].

[60] The red fines in Phoenix soils (as imaged by the OM) appear to be darker than near-surface airborne dust accumulated on the Phoenix magnets and significantly darker than high-altitude airborne dust [*Goetz et al.*, 2009]. The black sand particles have a varying surface roughness with localized distinct (green, red, or blue) glints that indicate the presence of small planar faces, possibly crystal facets. The brown sand particles are mostly translucent and have a smoother, glossy surface with specular reflections. Their translucence varies though in a wide range from almost transparent to dark brown (opaque) particles.

[61] Phoenix soils have also been compared to Gusev ripple soils (Serpent, El Dorado). The latter soils have a large abundance of sand-sized particles, but are somewhat depleted in 500 to 700 μm large sand grains. Phoenix soils appear to lack medium to large sand-sized particles in a wide size range (200–1000 μm). The virtual absence of such particles in Phoenix soils is difficult to prove. However, no such particle could be unambiguously identified in any RAC or SSI images.

[62] Both Gusev and Phoenix soil samples have a bimodal red albedo. The bright particles have a red albedo that is by a factor of 2~4 larger than that of the dark particles.

[63] PHX-OM images are the first (truly) microscopic images ever returned by a landed mission to Mars. Therefore no firm statement can be made on the potential global distribution of the sand-sized soil particles seen in those images. Based on color and surface texture, the black sand particles are tentatively interpreted as unweathered (or at most very weakly altered) basaltic (or mafic) lithic fragments that have been rounded by eolian transport. If true they would be similar to the larger El Dorado dune particles in Gusev crater [*Morris et al.*, 2008; *Ming et al.*, 2008].

[64] The black sand particles may be part of a global population of Martian particles that have been forming by ongoing sand abrasion of basaltic surface rocks in a dry environment and are moved across the planet by saltation. Alternatively, they may represent volcanic ash from the Tharsis region, or may be related to the dark circumpolar dunes [*Herkenhoff and Vasavada*, 1999; *Tanaka and Hayward*, 2008, *Tanaka et al.*, 2008]. All three scenarios would imply that these black sand particles survived long travel distances (larger than 500 km) and thus are resistant to mechanical breakdown. The latter property would also suggest that they are widely distributed across the surface of the planet. Additionally these particles should be composed of rather primitive basaltic material that has undergone less weathering than the other soil particle types.

[65] The brown sand particles are distinctly different from the black ones and must belong to a different class of soil particles. The following potential scenarios would be consistent with a common origin for the brown sand particles: (1) They may have been exhumed from the ice-rich subsurface by the Heimdal impact event or (2) they may be altered volcanic ash. According to the second scenario we would distinguish between a substantially altered and a (mostly) unaltered part of the ash, corresponding to the brown and black sand particles, respectively. The second scenario could also be related to the Heimdal impact event, as some short-lived hydrothermal activity may have driven aqueous weathering processes in the vicinity of the crater. Any combination of these two scenarios would be plausible. Both scenarios should produce a wide array of different particles, either because they were exhumed from different depths ranging from the near-surface to about one kilometer, or because they have reached different stages of alteration. Both scenarios would thus be consistent with the observed

particle diversity (see section 3.2) and would suggest that the brown sand particles are not as widespread as the black ones.

[66] We did not encounter clear examples where black and brown particles are part of larger "composite particles." A single blurry image of the strong magnet (sol 25, 6581, acquired prior to delivery of Rosy Red soil, not presented here) may show such a composite particle, but it is discarded because of its low technical quality. Finding such particles in statistically significant amounts might indicate a common source or source region for both types of grains. However, given the absence of such observations, both types of grains may have formed close in time and space by the same mechanism (impact, volcanism) or they may have formed independently of each other.

[67] Some of the described properties of the silt- and sand-sized grains in Phoenix soils can also be found in terrestrial palagonitic soils. As an example, the Hawaiian palagonitic soil referred to as HWMK1 [*Morris et al.*, 1990] contains black and orange tephra particles (sand sized) that appear to match to some degree the black and brown particles in Phoenix soils, respectively. The black particles in the Hawaiian soil are hard, dominantly crystalline, relatively unaltered and strongly magnetic, while the orange ones are more easily crushed, heavily altered and less magnetic.

[68] The model for the red fines is less speculative. Based on their spectral properties the red fines most likely belong to a global unit that comprises both airborne dust and bright surface soil. That type of material represents the most widespread alteration material on the surface of Mars and has been characterized by Earth-based telescopes ever since as well as Martian orbiters and landers. It may be the end product of a largely dry and extremely slow alteration of basaltic rocks, including those black sand particles that are amply discussed in the present paper. The color of the red fines is caused by the presence of nanophase ferric oxides [*Morris et al.*, 2006a, 2008]. The fine size fraction of the tephra that was discussed in the previous paragraph is a spectral analog for the red fines.

[69] The white fines occur as small flakes in the soil material. No data beyond color constrain the nature of these fines. They may contain several components such as carbonates, perchlorates, calcium sulfate, feldspar or even water ice. The latter option is unlikely, however, as water ice should have sublimed by the time OM images were acquired. Perchlorates [*Kounaves et al.*, 2010] may have formed in the atmosphere [*Catling et al.*, 2010], whereas carbonates [*Boynton et al.*, 2009] and postulated calcium sulfate [*Golden et al.*, 2009] may have formed at the landing site as a result of aqueous alteration. All potential whitish material taken together should make up considerably more material (at least 5 weight %) [*Boynton et al.*, 2009; *Hecht et al.*, 2009; *Kounaves et al.*, 2010] than the amount that actually can be identified in microscopic images (see Table 2). This indicates that most of this material is finely divided and distributed across the bulk volume of the soil.

[70] **Acknowledgments.** This research was supported in part by Deutsches Zentrum für Luft- und Raumfahrt e.V. (DLR) grant 50 QM 0602, the UK Science and Technology Facilities Council, the Wolferman Nägeli Foundation, and NASA/JPL. D. Parrat acknowledges a fellowship from the Swiss National Science foundation. R.V. Morris acknowledges support of the NASA Mars Phoenix Scout Mission Project and the NASA Johnson Space Center. M.B. Madsen, K. Leer, and L. Drube acknowledge support from the Danish Research Agency and from the Lundbeck Foundation. Discussions with R. Sullivan, Cornell University, on ripple types and associated soil particle sizes at the Gusev site were very inspiring. R. Bugiolacchi, Max Planck Institute for Solar System Research, helped with processing of some images.

References

Arvidson, R. E., et al. (2008), Spirit Mars Rover Mission to the Columbia Hills, Gusev crater: Mission overview and selected results from the Cumberland Ridge to Home Plate, *J. Geophys. Res.*, *113*, E12S33, doi:10.1029/2008JE003183.

Arvidson, R. E., et al. (2009), Results from the Mars Phoenix Lander Robotic Arm experiment, *J. Geophys. Res.*, *114*, E00E02, doi:10.1029/2009JE003408.

Bell, J. F., III, J. Joseph, J. N. Sohl-Dickstein, H. M. Arneson, M. J. Johnson, M. T. Lemmon, and D. Savransky (2006), In-flight calibration and performance of the Mars Exploration Rover Panoramic Camera (Pancam) instruments, *J. Geophys. Res.*, *111*, E02S03, doi:10.1029/2005JE002444.

Bell, J. F., III, M. S. Rice, J. R. Johnson, and T. M. Hare (2008), Surface albedo observations at Gusev crater and Meridiani Planum, Mars, *J. Geophys. Res.*, *113*, E06S18, doi:10.1029/2007JE002976.

Boynton, W. V., et al. (2009), Evidence for calcium carbonate at the Mars Phoenix landing site, *Science*, *325*, 61–64, doi:10.1126/science.1172768.

Cabrol, N. A., et al. (2008), Soil sedimentology at Gusev crater from Columbia Memorial Station to Winter Haven, *J. Geophys. Res.*, *113*, E06S05, doi:10.1029/2007JE002953.

Catling, D. C., M. W. Claire, K. J. Zahnle, R. C. Quinn, B. C. Clark, M. H. Hecht, and S. Kounaves (2010), Atmospheric origins of perchlorate on Mars and in the Atacama, *J. Geophys. Res.*, *115*, E00E11, doi:10.1029/2009JE003425.

Drube, L., et al. (2009), Magnetic and optical properties of airborne dust and settling rates of dust at the Phoenix landing site, *J. Geophys. Res.*, doi:10.1029/2009JE003419, in press.

Goetz, W., et al. (2005), Indication of drier periods on Mars from the chemistry and mineralogy of atmospheric dust, *Nature*, *436*, 62–65, doi:10.1038/nature03807.

Goetz, W., S. F. Hviid, K. M. Kinch, and M. B. Madsen (2008a), Magnetic properties results from surface landers and rovers, in *The Martian Surface: Composition, Mineralogy and Physical Properties*, edited by J. F. Bell III, pp. 366–380, Cambridge Univ. Press, New York, doi:10.1017/CBO9780511536076.017.

Goetz, W., et al. (2008b), The search for magnetic minerals in Martian rocks: Overview of the Rock Abrasion Tool (RAT) magnet investigation on Spirit and Opportunity, *J. Geophys. Res.*, *113*, E05S90, doi:10.1029/2006JE002819.

Goetz, W., et al. (2009), Martian airborne dust: How it forms and evolves. Near-surface versus high-altitude properties, paper presented at Mars Dust Cycle Workshop, NASA Ames Res. Cent., Mountain View, Calif., 15–17 Sept.

Golden, D. C., et al. (2009), Sulfur mineralogy at the Mars Pheonix landing site, *Lunar Planet. Sci., XL*, Abstract 2319.

Hapke, B. (1993), *Theory of Reflectance and Emittance Spectroscopy*, Cambridge Univ. Press, New York, doi:10.1017/CBO9780511524998.

Hecht, M. H., et al. (2008), Microscopy capabilities of the Microscopy, Electrochemistry, and Conductivity Analyzer, *J. Geophys. Res.*, *113*, E00A22, doi:10.1029/2008JE003077.

Hecht, M. H., et al. (2009), Detection of perchlorate and the soluble chemistry of Martian soil: Findings from the Phoenix Mars Lander, *Science*, *325*, 64–67, doi:10.1126/science.1172466.

Heet, T. L., R. E. Arvidson, S. C. Cull, M. T. Mellon, and K. D. Seelos (2009), Geomorphic and geologic settings of the Phoenix Lander mission landing site, *J. Geophys. Res.*, *114*, E00E04, doi:10.1029/2009JE003416.

Herkenhoff, K. E., and A. R. Vasavada (1999), Dark material in the polar layered deposits and dunes on Mars, *J. Geophys. Res.*, *104*, 16,487–16,500, doi:10.1029/1998JE000589.

Herkenhoff, K. E., et al. (2003), Athena Microscopic Imager investigation, *J. Geophys. Res.*, *108*(E12), 8065, doi:10.1029/2003JE002076.

Keller, H. U., et al. (2008), Phoenix Robotic Arm Camera, *J. Geophys. Res.*, *113*, E00A17, doi:10.1029/2007JE003044.

Kounaves, S. P., et al. (2010), Wet Chemistry Experiments on the 2007 Phoenix Mars Scout Lander mission: Data analysis and results, *J. Geophys. Res.*, *115*, E00E10, doi:10.1029/2009JE003424.

Landis, G. A., et al. (2006), Dust and sand deposition on the MER solar arrays as viewed by the microscopic imager, *Lunar Planet. Sci.*, *XXXVII*, Abstract 1932.

Leer, K., et al. (2008), Magnetic properties experiments and the Surface Stereo Imager calibration target onboard the Mars Phoenix 2007 Lander:

Design, calibration, and science goals, *J. Geophys. Res.*, *113*, E00A16, doi:10.1029/2007JE003014.
Leer, K., et al. (2009), Optical study of particles on Phoenix magnets, *Lunar Planet. Sci.*, *XL*, Abstract 1923.
Madsen, M. B., et al. (2003), Magnetic Properties Experiments on the Mars Exploration Rover mission, *J. Geophys. Res.*, *108*(E12), 8069, doi:10.1029/2002JE002029.
Madsen, M. B., et al. (2009), Overview of the magnetic properties experiments on the Mars Exploration Rovers, *J. Geophys. Res.*, *114*, E06S90, doi:10.1029/2008JE003098.
Maki, J. N., et al. (1999), The color of Mars: Spectrophotometric measurements at the Pathfinder landing site, *J. Geophys. Res.*, *104*, 8781–8794, doi:10.1029/98JE01767.
Ming, D. W., et al. (2008), Geochemical properties of rocks and soils in Gusev crater, Mars: Results of the Alpha Particle X-Ray Spectrometer from Cumberland Ridge to Home Plate, *J. Geophys. Res.*, *113*, E12S39, doi:10.1029/2008JE003195.
Morris, R. V., J. L. Gooding, H. V. Lauer, and R. B. Singer (1990), Origins of Mars-like spectral and magnetic properties of a Hawaiian palagonitic soil, *J. Geophys. Res.*, *95*, 14,427–14,434, doi:10.1029/JB095iB09p14427.
Morris, R. V., et al. (2006a), Mössbauer mineralogy of rock, soil, and dust at Gusev crater, Mars: Spirit's journey through weakly altered olivine basalt on the plains and pervasively altered basalt in the Columbia Hills, *J. Geophys. Res.*, *111*, E02S13, doi:10.1029/2005JE002584.
Morris, R. V., et al. (2006b), Mössbauer mineralogy of rock, soil, and dust at Meridiani Planum, Mars: Opportunity's journey across sulfate-rich outcrop, basaltic sand and dust, and hematite lag deposits, *J. Geophys. Res.*, *111*, E12S15, doi:10.1029/2006JE002791.
Morris, R. V., et al. (2008), Iron mineralogy and aqueous alteration from Husband Hill through Home Plate at Gusev crater, Mars: Results from the Mössbauer instrument on the Spirit Mars Exploration Rover, *J. Geophys. Res.*, *113*, E12S42, doi:10.1029/2008JE003201.
Pike, W. T., et al. (2009), Fractal analysis of the microstructure of the Martian soil at the Phoenix landing site, *Lunar Planet. Sci.*, *XL*, Abstract 1909.
Putzig, N. E., and M. T. Mellon (2007), Apparent thermal inertia and the surface heterogeneity of Mars, *Icarus*, *191*, 68–94, doi:10.1016/j.icarus.2007.05.013.
Reid, R. J., et al. (1999), Imager for Mars Pathfinder (IMP) image calibration, *J. Geophys. Res.*, *104*, 8907–8925, doi:10.1029/1998JE900011.
Reynolds, R. O., R. D. Tanner, and S. Albanna (2008), Qualification of LEDs for cameras on NASA's Phoenix Mars Lander, in *Nanophotonics and Macrophotonics for Space Environments II*, edited by E. W. Taylor and D. A. Cardimona, *Proc. SPIE*, *7095*, 70950A-70950A-12, doi:10.1117/12.806208.
Smith, P., et al. (2009), H_2O at the Phoenix landing site, *Science*, *325*, 58–61.
Sullivan, R., et al. (2008), Wind-driven particle mobility on Mars: Insights from Mars Exploration Rover observations at "El Dorado" and surroundings at Gusev Crater, *J. Geophys. Res.*, *113*, E06S07, doi:10.1029/2008JE003101.
Sykulska, H. M., W. T. Pike, and S. Vijendran (2009), Microscopy Analysis of the Salt Content of Soil and Dust at the Phoenix Landing Site, *Lunar Planet. Sci.*, *XL*, Abstract 2366.
Tanaka, K. L., and R. K. Hayward (2008), Mars' north circum-polar dunes: Distribution, sources, and migration history, in *Planetary Dunes Workshop: A Record of Climate Change*, *LPI Contrib., 1403*, Abstract 7012.
Tanaka, K. L., J. A. P. Rodriguez, J. A. Skinner Jr., M. C. Bourke, C. M. Fortezzo, K. E. Herkenhoff, E. J. Kolb, and C. H. Okubo (2008), North polar region of Mars: Advances in stratigraphy, structure, and erosional modification, *Icarus*, *196*, 318–358, doi:10.1016/j.icarus.2008.01.021.
Wentworth, C. K. (1922), A scale of grade and class terms for clastic sediments, *J. Geol.*, *30*, 377–392, doi:10.1086/622910.

R. E. Arvidson, Department of Earth and Planetary Sciences, Washington University in St. Louis, St. Louis, MO 63108, USA.
J. F. Bell III, Department of Astronomy, Cornell University, Ithaca, NY 14853, USA.
D. Blaney, M. H. Hecht, and J. M. Morookian, Jet Propulsion Laboratory, California Institute of Technology, Pasadena, CA 91125, USA.
B. J. Bos, NASA Goddard Space Flight Center, Greenbelt, MD 20771, USA.
L. Drube, K. Leer, and M. B. Madsen, Niels Bohr Institute, University of Copenhagen, DK-2100, Copenhagen, Denmark.
M. R. El Maarry, W. Goetz, S. F. Hviid, H. U. Keller, R. Kramm, and W. J. Markiewicz, Max Planck Institute for Solar System Research, Max-Planck-Str. 2, D-37191 Katlenburg-Lindau, Germany. (goetz@mps.mpg.de)
E. Hemmig, W. T. Pike, H. Sykulska, and S. Vijendran, Department of Electrical and Electronic Engineering, Imperial College, London SW7 2AZ, UK.
J. Marshall, SETI Institute, 515 N. Whisman Rd., Mountain View, CA 94043, USA.
R. V. Morris, NASA Johnson Space Center, Houston, TX 77058, USA.
D. Parrat, Institute of Microtechnology, University of Neuchâtel, CH-2000 Neuchâtel, Switzerland.
R. Reynolds, P. H. Smith, R. Tanner, P. Woida, and R. Woida, Lunar and Planetary Laboratory, University of Arizona, Tucson, AZ 85719, USA.
U. Staufer, Micro and Nano Engineering Laboratory, Delft University of Technology, NL-2600 AA Delft, Netherlands.